PRECISION ENGINEERING CENTER

2004 INTERIM REPORT
September 2004

Sponsors:

3M Corporation
Los Alamos National Laboratory
National Science Foundation
Precitech Precision, Inc.
Sandia National Laboratory
Vistakon, Johnson & Johnson Vision Care Inc.

Faculty:

Thomas Dow, Editor
Greg Buckner
Jeffrey Eischen
Paul Ro
Ronald Scattergood
David Youden

Graduate Students:

David Brehl
Brett Brocato
Nathan Buescher
Karalyn Folkert
Karl Freitag
Simon Halbur
Tim Kennedy
Witoon Panusittikorn
Travis Randall
Yanbo Yin

Undergraduate Students:

Anthony Wong

Staff:

Ken Garrard
Lara Masters
Alexander Sohn

TABLE OF CONTENTS

FABRICATION

ACTUATION

METROLOGY

1 TWO-AXIS FORCE-FEEDBACK DELFECTION COMPENSATION OF MINIATURE BALL END MILLS

Karl Freitag
Graduate Student
Thomas Dow
Professor
Department of Mechanical and Aerospace Engineering

1.1 INTRODUCTION

The fabrication of injection molding dies is one application of interest for this research. These dies are machined from hard steels (Heat treated to ~ 60 Rockwell C) to provide durable, wear resistant dies. Manufacture of these dies containing small features or precision surfaces require the use of tools with small radii. The tools required for such machining (Diameters < 1.0 mm) termed miniature tools and are the focus of this research. These tools are available in several different shank lengths to accommodate various applications and die geometries. Figure 1 contains a photograph of the 0.8 mm diameter miniature ball end mills used. The tools are made of tungsten carbide with a titanium aluminum carbide coating. Although the tool material is very strong, the thin geometry of these tools results in low tool stiffness (0.2 N/μm and less) which becomes a significant factor machining heat treated steels. Deflections of these tools under low (10N) cutting forces can produce part errors of 50 μm with a 4.0mm shank tool. The primary goal of this research is to reduce tool deflection errors to ± 2 μm, through the use of force-feedback machining.

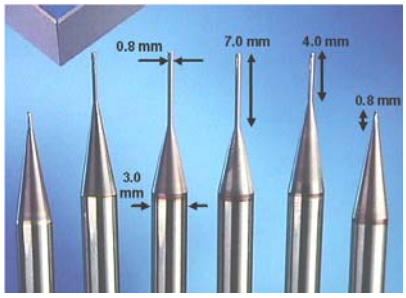

Figure 1. Miniature Ball End Mills

1.2 DESCRIPTION OF APPARATUS

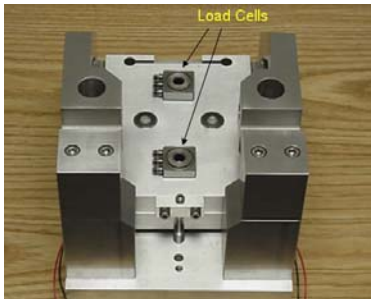

Figure 2. Force Measurement Platform

The two axis force feedback actuator was designed using piezo electric actuators to produce the tool displacement, flexures to guide the displacements, and capacitance gages to provide closed loop feedback. The spindle actuator assembly contains two Kistler model 9251 piezo electric force transducers to measure the real time cutting forces. The force transducers are located directly beneath an air bearing machining spindle and above the actuation platform (See Figure 2). The load cell

location was moved from the previous single axis actuator design where the actuation forces of the piezoelectric actuator pass thru the force transducer. Separation of this force loop allows more accurate measurement of the cutting forces with minimal interference from the actuation forces. The two load cells are spaced evenly about the spindle's center of gravity to reduce the effects of in-phase or out-of-phase spindle vibration in processing of the force signal. Beneath the force measurement platform are two piezo electric actuators used to produce the horizontal and vertical tool motion. See 2004 Annual Report for a detailed description of the flexure actuation. The complete apparatus is shown on the right in Figure 3.

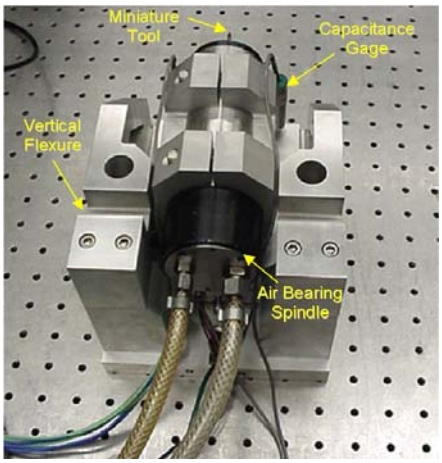

Figure 3. Spindle Actuator Assembly

1.3 MULTIVARIABLE CONTROL

The force feedback spindle actuator is a two-input two-output system where the displacement at each piezo stack contributes to both the horizontal and vertical tool position. Control of the actuator is achieved through decoupling of the horizontal and vertical dynamics. Proportional Integral (PI) control is used to control the horizontal and vertical systems separately and then recombined to solve for the individual voltage to each piezo. The horizontal controller produces the differential voltage between the two piezos while the vertical controller produces a sum. The command following of the two-axis actuator was evaluated with an 8μm square profile. The square motion profile below in Figure 4 (Left) was positioned in a total time of 500ms. The complete force feedback control algorithm is shown below in Figure 4 (Right) where the

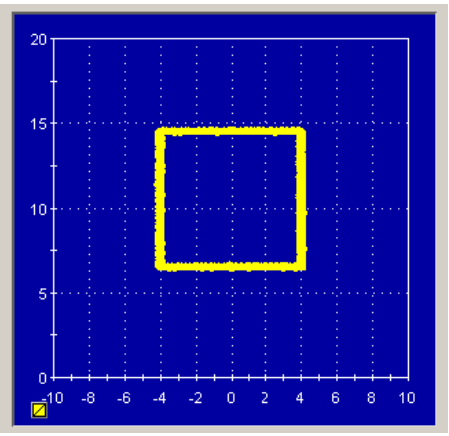

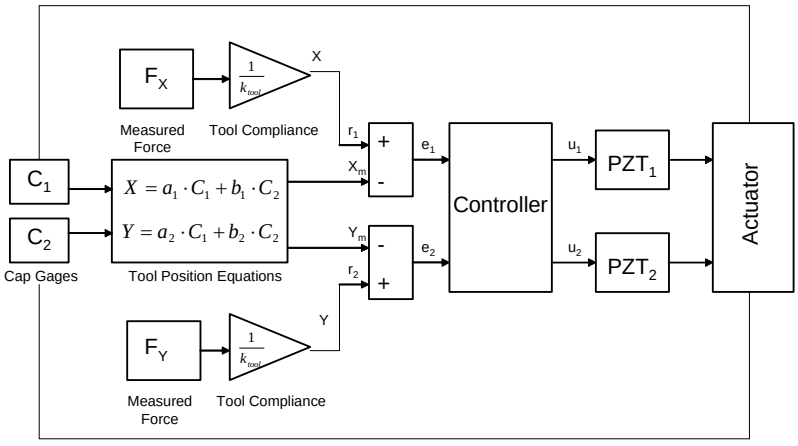

Figure 4. Command following, Tool position (μm), Force-Feedback Block Diagram (Right)

horizontal and vertical tool forces are first measured to produce a desired horizontal and vertical

tool position. The two axis controller then positions the tool to the desired position using capacitance gage closed loop feedback. Step response for a horizontal and vertical 2µm step are displayed below in Figure 5 below.

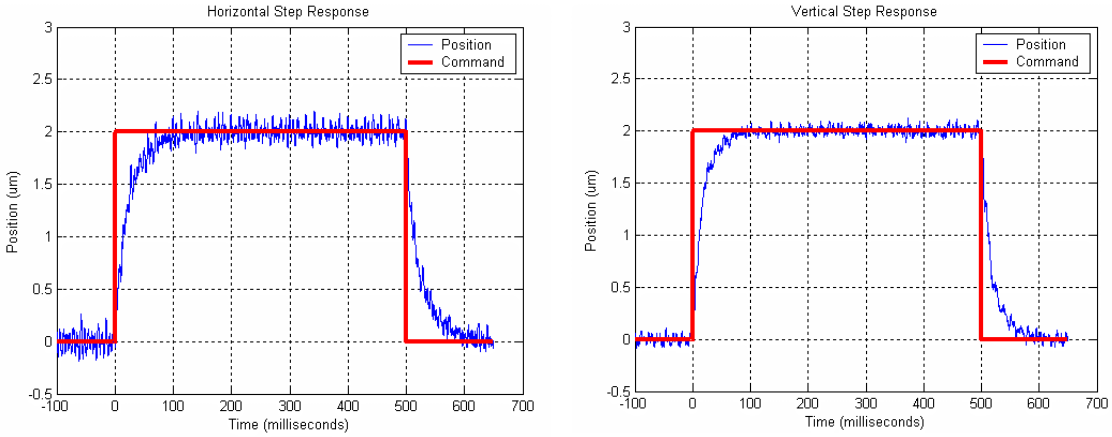

Figure 5. Horizontal Step Response (Left), Vertical Step Response (Right)

1.4 EXPERIMENTAL VERIFICATION

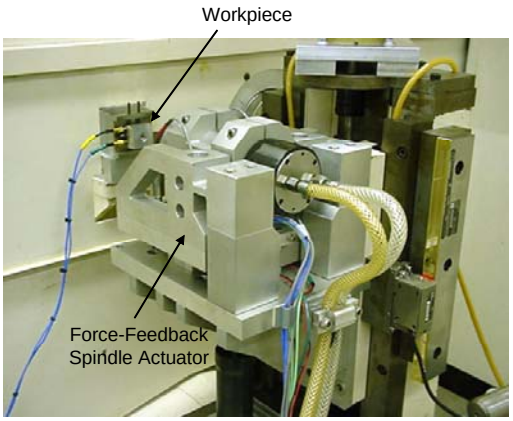

Figure 6. Experimental Set-Up

To exercise the two axis force feedback actuator, two 3-dimensional surfaces were raster cut using the force feedback spindle and a fixed spindle for comparison. The machining spindle was mounted on the Y (Vertical) axis of the Nanoform 600 DTM (Figure 6). The parts were raster cut feeding left to right using the Y-Axis to provide the cross feed. The tool path in XYZ coordinates for the raster cut sequence is shown in Figure 7. A five millimeter diameter hemisphere was cut using both the force feedback spindle and a fixed spindle for comparison. A photograph of the raster cut hemisphere is shown in Figure 8. Due to probe interference near the walls of the hemisphere, accurate measurements were difficult to obtain and a four sided frustum profile was chosen to improve measurement capability.

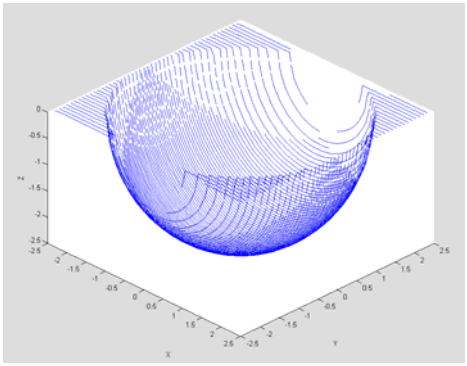

Figure 7. X,Y,Z Raster Tool Path

Figure 8. 5mm Hemisphere

The dimensions of four sided frustum (Figure 9) are a 5mm square with a 1mm square located 1.5mm deep. Measurement of the final part is performed by scanning the part surface with the Talysurf profilometer. In the machining of this geometry, the tool forces result in deflection of the tool in each direction (Figure 10). Comparison between the force feedback spindle and the fixed spindle part measurements (Figure 11) show an average improvement in part geometry of around 15μm over the uncompensated profiles. The measurements in Figure 9 are correspond to the inside frustum wall at the tool location from Figure 8.

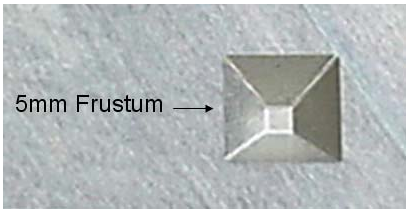

Figure 9. 5mm 4-Sided Frustum

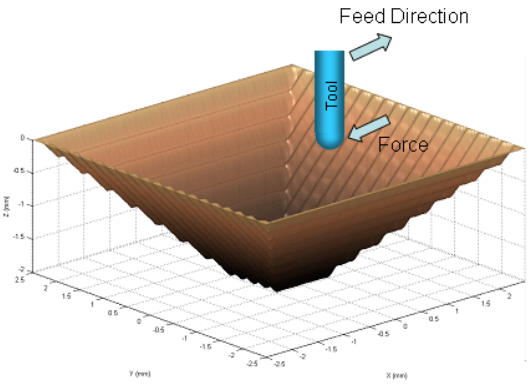

Figure 10. Feed Direction and Tool Force Direction

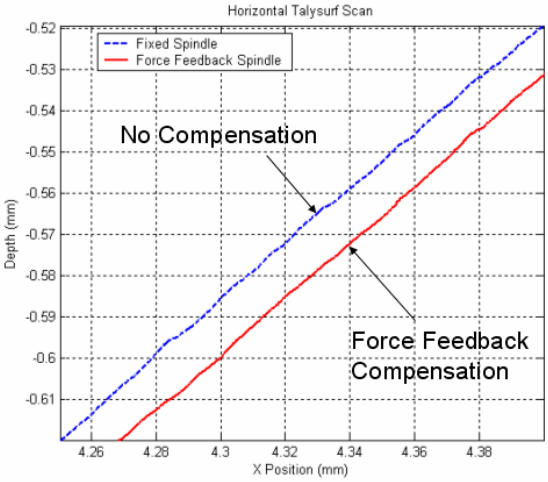

Figure 11. Part Measurement Comparison

The machining parameters of the four-sided frustum were first a rough cut using a cross-feed (ΔY) of 250μm and increasing depth (ΔZ) of 200μm until the rough cut depth of 1.2mm is achieved. A federate of 50mm/min is used for both the rough cut and final pass. The final pass then contains a 300μm depth of cut and 100μm cross-feed (ΔY) to obtain the final part geometry.

1.5 CONCLUSIONS

The mechanical design of the 2-axis system allows the machining force in each direction to be independently measured and the tool end positioned to compensate for the resulting deflection. Two 3-axis load cells are used to measure the force and the correction is made with two piezoelectric actuators that use capacitance gages for position feedback. Techniques for capturing the peak force, using that force along with the tool compliance to create a positioning error, comparing that error with the cap gage readings and sending the filtered commands to the actuators have been developed and demonstrated. Two machined features are described: a 5 mm radius hemisphere and a 5 mm wide 4-sided frustrum. Each surface was machined using a raster scan technique and the magnitude and direction of the machining forces were measured and tool

deflection compensated. Error in final part geometry due to tool deflection was reduced by 15μm through the implementation of force feedback compensation.

.

REFERENCES

1. Dow, T., Miller E., Garrard K., Sohn A., Wright, T. "Compensation of Tool Force in Small Diameter End Mills," ASPE Proceedings, Vol. 20, pp. 546-550 and to be published in Precision Engineering in 2003

2. Clayton , S. , "Force Modeling and Deflection Compensation of Miniature Ball End Mills," MS Thesis, North Carolina State University, 2003.

3. Hood, D, "Force Feedback Control of Tool Deflection in Miniature Ball End Milling," MS Thesis, North Carolina State University, 2003.

4. Miller, E., "Deflection Prediction and Error Correction of High Speed Miniature Milling Tools," MS Thesis, North Carolina State University, 2000.

5. Smith, S., Flexures: Elements of Elastic Mechanisms, Gordon and Breach Science Publishers, 2000

6. Lobontiu, N., Compliant Mechanisms: Design of Flexure Hinges, CRC Press, 2003.

7. Drescher, J. D., "Tool Force Measurement in Diamond Turning," MS Thesis, North Carolina State University, 1989.

8. Arcona, C., "Tool Force, Chip Formation and Surface Finish in Diamond Turning," Ph.D. Dissertation, North Carolina State University, 1996.

9. Minor, P., "Tool Wear and Tool Forces in High Speed Machining of Aluminum," MS Thesis, North Carolina State University, 1998.

10. Altintas, Y., Manufacturing Automation: Metal Cutting Mechanics, Machine Tool Vibrations, and CNC Design, Cambridge University Press, 2000.

2 SURFACE DECONVOLUTION FOR DIAMOND TURNING

Witoon Panusittikorn
Post-Doc Researcher
Kenneth Garrard
Precision Engineering Center Staff
Thomas A. Dow
Professor
Department of Mechanical and Aerospace Engineering

2.1 INTRODUCTION

The use of a fast tool servo (FTS) to create non-rotationally symmetric optical surfaces is growing. However, this device can introduce amplitude and phase errors to the commanded signal resulting in form errors on the machined part. The goal of this research effort is to use an understanding of the dynamics of the FTS to create open-loop modifications of the input signal that will correct these errors. Deconvolution is a mathematical procedure that can produce a modified input to reverse the effects of attenuation and phase if the impulse response of the dynamic system is known. Since this modified command is not calculated from the position feedback signal, there is no delay in the response. When applied to a Variform long-range FTS, the result is dramatic improvement in the following error especially for high frequency motion [1]. To test this technique, an off-axis spherical surface feature was first selected because of the perceived ease of measurement using a laser interferometer. Unfortunately, other issues such as the correction for the nose radius of the tool complicated the interpretation of the measured results. As a result, a new feature in the form of a cosine, has been used to validate the technique.

2.2 COSINE GROOVE

A cavity with a cosine wave cross section was used as the new test shape to verify the deconvolution technique. The shape is in Figure 1 where a full period cosine wave is smoothly integrated into a flat surface. As a result, no sharp corners exist in the tool trajectory and, since the cavity has a constant

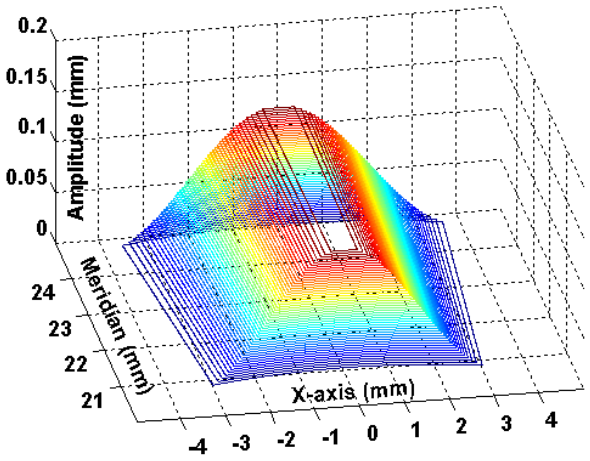

Figure 1. A cylinder cavity with a full cosine wave cross section

depth, the same tool excursion can be replicated for every revolution. Turning this feature does not need tool radius compensation so the input command modification technique can be clearly validated without any influences of other corrective schemes.

2.3 CREATING AN INPUT SIGNAL

Deconvolution The desired shape is an 18-degree wide, off-axis cosine groove with a 240 μm peak-to-valley sag. If machined at 561 rpm, the dominant frequency will be 187 Hz[1], which is close to the peak of the gain response of the Variform FTS shown in Figure 2. At this frequency, the output trajectory will be amplified by 10% and delayed by 52^o resulting in a significant path difference with respect to the desired cosine wave. Block deconvolution with the overlap-add method [2] was used with the inverse dyanamics filter to modify the designated tool path. The operation was carried out in time domain where a desired excursion was segmented and individually convoluted with the equivalent inverse dynamics filter.

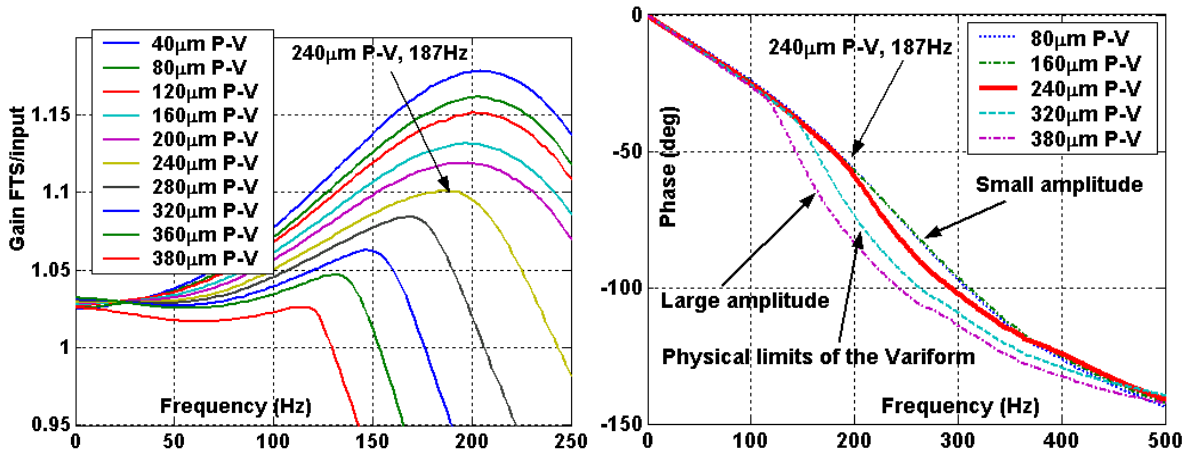

(a) Gain response (b) Phase response

Figure 2. The cosine profile of the test part has a frequency component close to the peak of the gain response and near the physical limits of the Variform

The simulated output trajectory (points in Figure 3) associated with a modified input command (circles) was close to the desired path (squares). The estimated error (a dash line) was less than 200 nm P-V.

Experimental Verification The modified input signal was then experimentally verified by driving the Variform FTS with it mounted on an optical table and using a distance-measuring laser interferometer to measure the displacement of the tool. Figure 4(a) illustrates the agreement of the FTS motion (x marks) and that of the simulation (in Figure 3.) The output trajectory was in-phase and the path difference was $\pm 1\,\mu$m near the peak and 8μm at the edges.

[1] If machined continuously around the part, there would be 20 waves and the temporal frequency would be 187 Hz.

The mismatch between the gain response used in the deconvolution operation and the actual response of the FTS may cause the path difference of the actual tool trajectory larger than that of the model. On the other hand, the tool trajectory (x marks in Figure 4b)) associated with an unmodified signal was, as expected, 10 μm bigger, and 52^o out of phase with respect to the desired path (a solid line). The dynamic response of the Variform caused a sinusoidal profile of the path difference (a solid line) with a magnitude of 225 μm P-V.

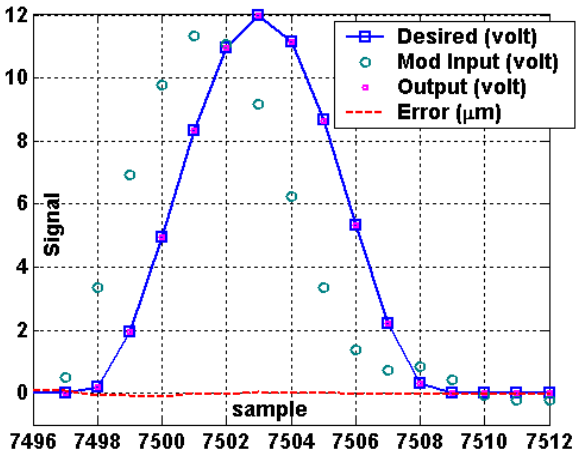

Figure 3. A simulated output tool path associated with a modified input command signal yielded an error of 200 nm P-V

Since the Variform was operating close to its maximum speed, the velocity was plotted to determine whether the operation was beyond the linear boundary of the FTS. If a tool excursion is a cosine wave, its velocity (or derivative) is a sine wave. In Figure 5(a) shows the distorted sine wave of the velocity profile and indicates that the FTS was performed within its limits; that is, less than 140 mm/sec. The unmodified excursion, on the other hand, exhibited a more a distorted wave and the tool speed (in Figure 5(b)) exceeded the linear range. This means that the input command modification technique can extend the usable bandwidth of the Variform.

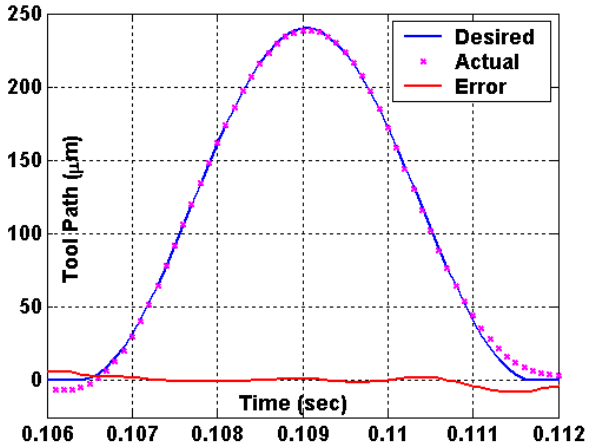

(a) Path difference associated with the deconvoluted input command

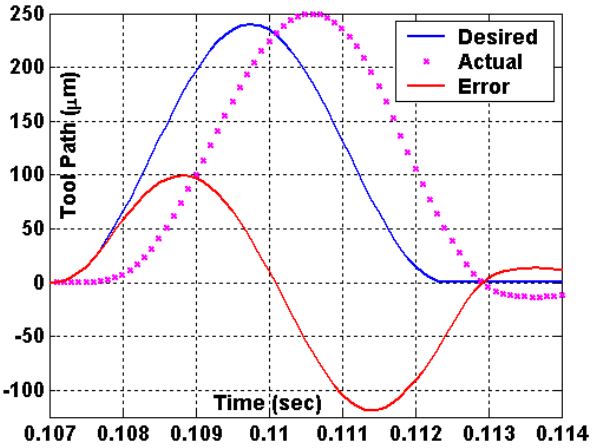

(b) Path difference associated with the unmodified input command

Figure 4. Comparison of the path differences associated with the modified and unmodified input commands

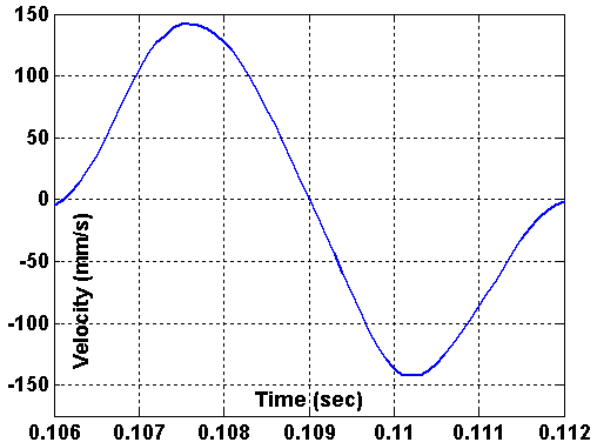

(a) A twisted sinusoidal velocity of the modified tool path

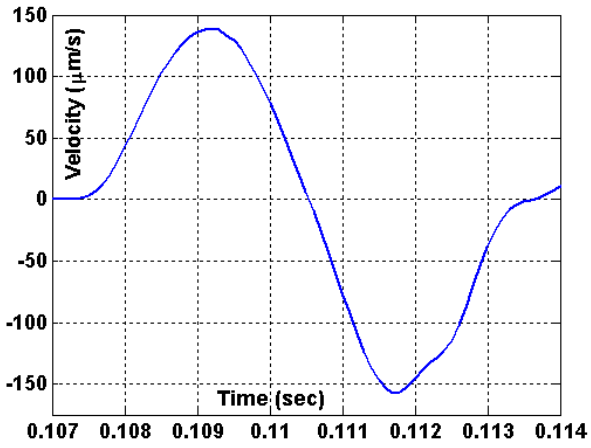

(b) A more distorted velocity profile of the unmodified path

Figure 5. The velocity profiles of the modified and unmodified tool path

2.4 MACHINED FEATURES

The cylindrical cavity with a cosine cross section profile was fabricated into a copper blank. The location of the desired machined feature was created at 0^o with respect with the reference flat. In Figure 6, the cosine groove closest to the outside of the copper blank was machined using the modified input command while the surface close to the center was machined with the unmodified input command.

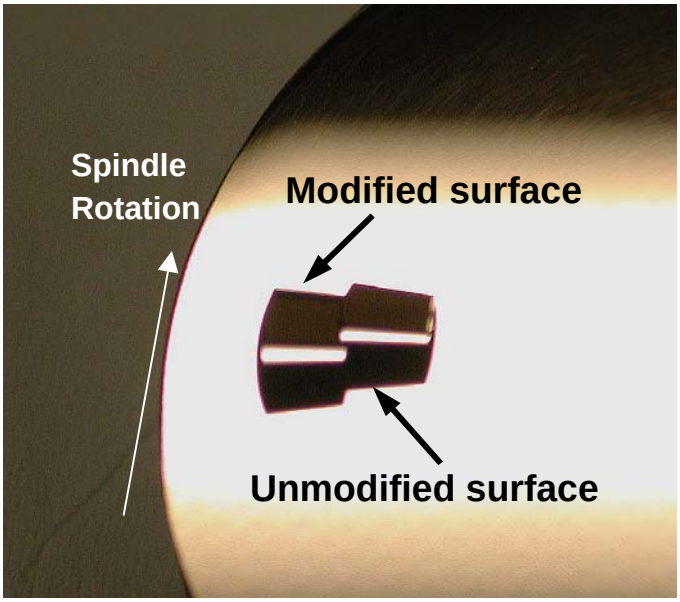

Figure 6. The machined surface associated with the modified and unmodified input

A comparison of the form errors between modified and unmodified surfaces was made using the Talysurf profilometer and the phase angles between the machined surfaces were measured using a microscope with linear scales on the cross slides. This technique located the features in the cartesian coordinates which were then transformed to the polar coordinate r and θ. The profile of the machined surface associated with the deconvoluted input command (measured along the trace (A) in Figure 7) is depicted as a solid line in the top graph of Figure 8(a), and the profile of the unmodified surface (measured along the trace (B)) is illustrated in Figure 8(b). The path differences with respect to the desired surface profile shown in the bottom graphs of both Figure 8(a) and (b) show that the unmodified surface was 50^o out of

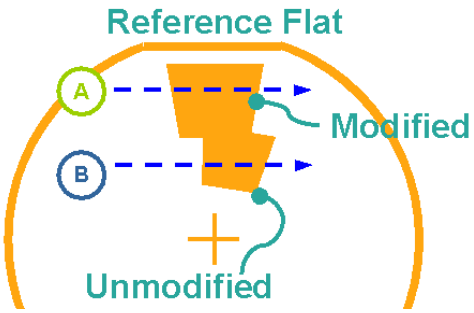

Figure 7. The profile measurement is parallel to the reference flat

phase resulting in a path difference of 122 μm P-V. The deconvoluted surface, shown in Figure 8(a), was in-phase. As a result, there was a significant reduction in form errors - two orders of magnitude down to 4 μm P-V as shown in the difference graph at the bottom of Figure 8(a). The surface was less than the commanded depth by 10 µm or about 4%. This difference could be the result of a touch off problem or a gain issue and additional experiments are planned to evaluate the cause. The largest difference between the modified and unmodified is the phase but if that alone were corrected, there would still be error in the shape of the surface created that the deconvolution process corrects.

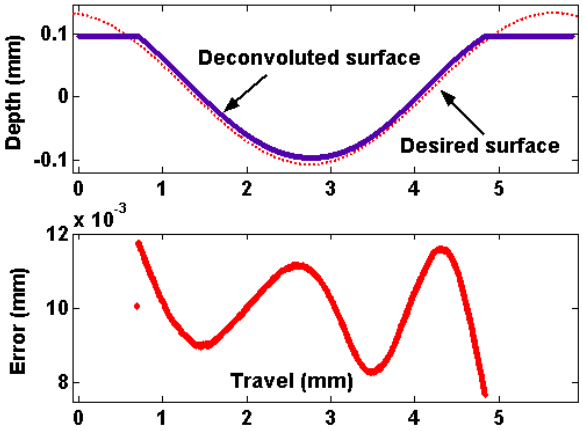

(a) Measured surface profile associated with the modified input command

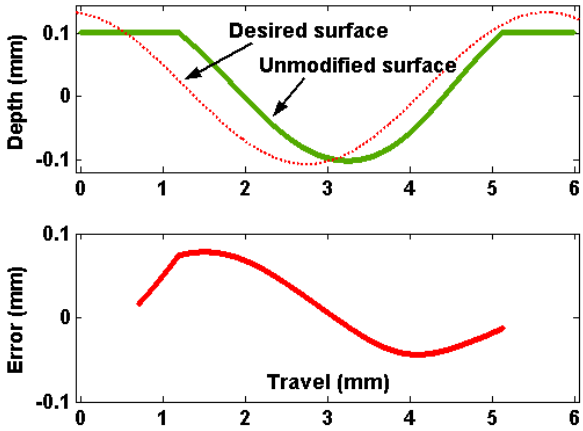

(b) Measured surface profile associated with the unmodified input command

Figure 8. The surface profile measurements of the modified and unmodified surfaces

2.5 CONCLUSION

The modified input signal created by the deconvolution technique improves the form fidelity of a machined surface when compared to that of the unmodified signal. The figure errors can be reduced by two orders of magnitudes due mostly to the correction of the phase errors. This result is true even if the machining conditions do not exactly match those designated. The machining experiments corroborate the simulated results and the tool path measurements using the laser interferometer when the Variform is mounted on an optical table. The results are also superior to those obtained if the phase and gain were adjusted based on the value at the operating frequency because the shape of the desired input command will not be correct. The shape of the input command signal must be modified to yield the output tool path close to the desired excursion.

3 MICRO-MACHINING USING ELLIPTICAL VIBRATION ASSISTED MACHINING

Brett Brocato
Graduate Student
Alex Sohn
Precision Engineering Center Staff
Thomas Dow
Professor
Department of Mechanical and Aerospace Engineering

3.1 INTRODUCTION

This paper demonstrates the effectiveness of a new machining process[1] that can be used to create three-dimensional micro-mechanical, micro-optical and micro-fluidic devices. Current MEMS manufacturing techniques like semiconductor lithography and LIGA suffer from high costs and long lead time for prototyping or short production runs. While micromachining is not what most people think of for creating microstructures, it has the potential for low-cost and fast manufacture of microstructures especially for molding tools [1]. Mechanical milling has been used for making micro-scale 3-D structures, but tool runout relative to feature size becomes worse as tool diameter decreases to produce smaller features. Tool deflection also increases as tool diameter decreases because of the lack of tool stiffness. The non-rotating tool described will reduced the minimum feature size possible while producing optical quality surface finish.

3.2 EXPERIMENTAL APPARATUS

A Diamond Turning Machine (DTM) (NanoForm 600) and a piezoelectric tool servo (UltraMill) are married into a fabrication system that significantly improves the feature resolution of micromachined components. The UltraMill is mounted on a vertical axis that was added to the 2-axis DTM machine as shown in Figure 1. Also on

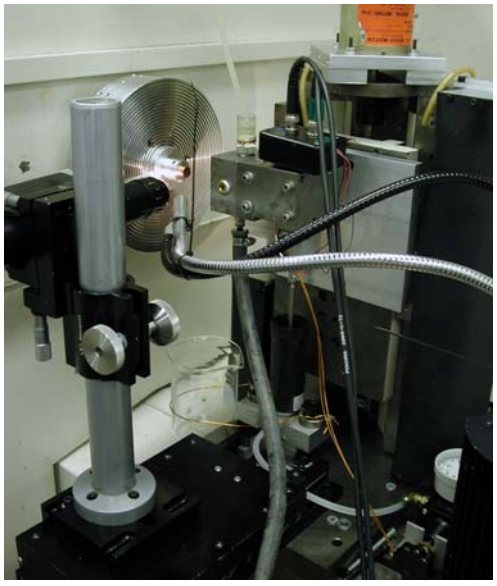

Figure 1. UltraMill mounted on the DTM

[1] Project funded in part by NSF under contract # DMI-0115175 monitored by G. Hazelrigg

the Y-axis is the telescope used to find the surface and the auxiliary tool used to planarize the surface. To create the 3D MEMS devices, the tool is raster scanned over the face of the part using X axis as the scan axis, the Y as the cross-feed axis and the Z to change the depth of cut. An alternate orientation is mounting the UltraMill on the spindle and the part on the Y-axis. The spindle can then be rotated to hold the cutting tool tangent to the cutting direction as the three axes move the part. The X and Z slides of the DTM have hydrostatic oil bearing slides and are driven by DC motors with ball screws. Position feedback is provided by differential laser interferometers with 1.25 nm positioning resolution. The vertical slide (Y) that supports the UltraMill (or the workpiece) is supported by hydrostatic air bearing, driven by a DC motor and ball screw with a high resolution (1 nm) linear encoder for positioning feedback. A Delta-Tau UMAC controller drives the positioning system.

Vibrating Tool Holder - UltraMill To create the tool motion, a high-speed piezoelectric actuator called the UltraMill is used. The concept behind this design was to create an adjustable design where the size, shape and frequency of the tool motion could be easily changed. A tool holder is preloaded against a pair of high-voltage piezoelectric stacks as shown in Figure 2. By driving the two stacks with sine and cosine waveforms, an elliptical tool path is created with the size of the major and minor axes depending on the spacing between stacks, the distance from the tool to the top of the stacks and the amplitude of the actuators. By changing the amplitude and phase of the drive signals, a range of tool paths from nearly linear to circular can be created.

A photograph of two generations of the vibrating tool design is also shown in Figure 2. The UltraMill is shown in the foreground with an earlier slower speed design in the background. The UltraMill uses triangular cross-section stacks and a hollow alumina tool holder (weight < 3 gm). A circular titanium diaphragm is mounted at the end of the housing that both seals the housing around the ceramic tool holder and preloads the stacks. The diamond tool[2] is glued to the end of the ceramic holder. The structure was designed to be light and stiff and lowest natural frequency is on the order of 10 KHz. The actuators have a length of 24 mm, a maximum stroke of 22 μm. The maximum excursion for the elliptical motion was a major axis of 52 μm, a minor axis of 8.5 μm and a total size of 104x17 μm measured at 600 v and 4 KHz. While the UltraMill can operate in a frequency range from 1-5 Khz, one of the challenges is cooling the stacks. The cooling system uses a temperature-controlled dielectric fluid pumped into the housing as shown

[2] The diamond tool is 1x1x5 mm in size and was supplied, polished and mounted by Chardon Tool

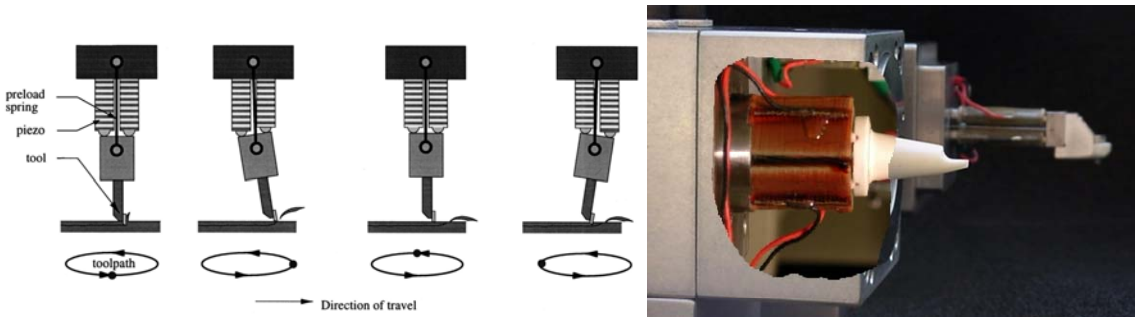

Figure 2. Concept of the Ultramill (left) and photograph of the two prototypes developed (right) in the cutaway in Figure 2. This system allows the UltraMill to operate continuously at 4000 Hz.

Tool Motion The relationship between the process variables (vibration frequency, amplitude, workpiece speed, depth of cut) are defined in Figure 3. In the case of elliptical tool motion coupled with the linear motion of the workpiece, the dynamic location of the tool edge (x,y) is:

$$x(t) = V_w \ \ t + a\cos(\omega \ t) \quad (1)$$

$$y(t) = b \ \ (1 + \sin(\omega \ \ t)) - d \quad (2)$$

where V_w is the workpiece speed, a and b are the major and minor axes of the ellipse, ω is the frequency of vibration, d is the depth-of-cut and t is time. Figure 3 can be used to illustrate the important parameters of the process [2]; two cycles of the tool are shown and the emphasis will be on the second cycle - a dotted line. This cycle defines the steady-state motion that removes material from the workpiece. Earlier publications on this technique have emphasized the parameters that control the material removal process but the emphasis here is the geometric features produced.

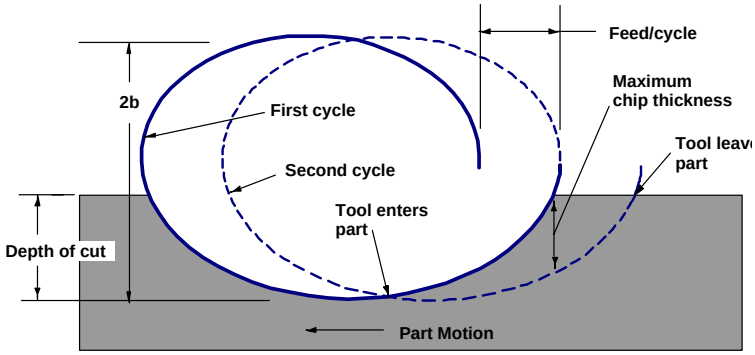

Figure 3. Elliptical tool motion superimposed on part motion.

Surface Features The motion of the diamond tool in the UltraMill produces a series of scalloped features that are elliptical (UltraMill motion) in the cutting direction and circular (tool nose radius) perpendicular to that direction. Thus each scallop has a "characteristic" shape that is a function of the

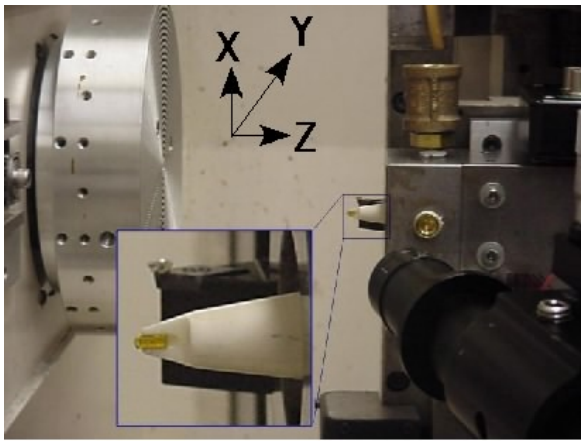

Figure 4. Closeup of the tools on Y axis

depth of cut and the feed rate in both the cutting direction and the cross feed direction. By choosing the tool nose radius and the depth of cut, different characteristic features can be created and become the building blocks for the surface features created. For example, a 1 mm radius diamond tool operating at the depth of cut of 500 nm with the UltraMill parameters a = 20 μm and b = 4 μm, will produce a characteristic feature with a length of 19 μm and a width of 63 μm for a L/W ratio of 3.25. If the tool nose radius is changed to 50 μm, the length remains unchanged and the width changes to 7 μm for a L/W of 0.75. The surface finish is controlled by the up-feed rate (part speed/UltraMill frequency) and by the cross-feed rate (spacing of scan lines). Surfaces finish better than 20 nm RMS have been created.

Operating Procedure The UltraMill is mounted on the vertical Y-axis as shown in Figure 4 which in turn is mounted to the Z-axis that moves in the direction of depth of cut. The part is mounted on the spindle whose slide moves in the X-direction. An auxiliary diamond tool is mounted next to the UltraMill on the Y-slide as shown in the inset in Figure 4. It is used to face off the test part to make its face in an X-Y plane and guarantee uniform depth of cut over the part. Once the part is faced, the spindle is locked and the UltraMill is touched off to start the machining process. The touch off process is done with the UltraMill operating at equilibrium temperature to deal with the thermal effects of the actuator operation. A long-range zoom microscope (20-130 X) is used to observe the generation of chips from the UltraMill when the surface is reached. The touch off procedure can find the surface to less than 0.5 μm. The features were machined using the X-axis to move the part under the vibrating tool with the Z-axis setting the depth of cut. The structures were raster scanned by cutting in the X-direction, retracting in the Z-direction, indexing in the Y-direction and returning to the start of the X scan.

3.3 PROGRAMMING MEMS FEATURES

The surfaces to be created can be grooved features or 3D shapes. Different programming techniques have been investigated including mathematical description of specific part features, automatic tool path generation from scanned images and CAM software. One complication is the size of the “characteristic” feature created by the UltraMill as discussed above. As the tool depth is increased, the width of the feature also increases. So if a recessed feature is desired, the scan definition must be modified to account for this change in width.

3.4 EXPERIMENTAL RESULTS

Grooves Figure 5 shows the results of a series of grooves machined with the UltraMill on a aluminum substrate. The difference in the two micrographs is the depth of cut. When the depth is less than the minor axis of the tool motion ellipse, the chips are discontinuous and if larger, they stay attached. However, the circular nose radius and the tool path combine to make the depth of cut approach zero at the edges of the groove. Notice that in Figure 5(b), the chip are

transparent to the SEM beam indicating a thickness less than 20 nm. As a result of the small chip size the motion of the tool, a remarkable lack of burring occurs when using the UltraMill. This is a profound advantage of other micromachining techniques.

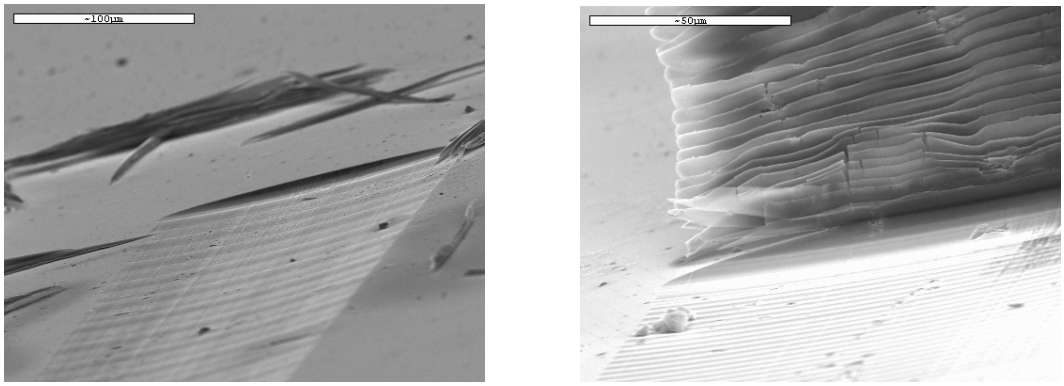

(a)1.3 µm depth (450x) (b) 8 µm depth (1000x)

Figure 5. SEM micrographs of groove and chip geometry (ellipse a = 20 µm, b = 4 µm)

3D Features Sub-millimeter features were machined to demonstrate the capabilities of the UltraMill fabrication process. The shape chosen was the angstrom symbol used in the PEC logo. The tool had a 1 mm nose radius and the desired feature height was 500 nm. The feature was machined on a copper substrate as shown in Figure 6 and the size of the image is 0.9 mm wide by 0.6 mm high. The height of the features is approximately 350 nm, slightly less than desired. It is also very uniform over the area, which is a testament to the excellent temperature control of the UltmaMill. The part was programmed with 137 scans and the fabrication time was less than 15 minutes. Smaller tool radii will permit smaller areal features to be generated.

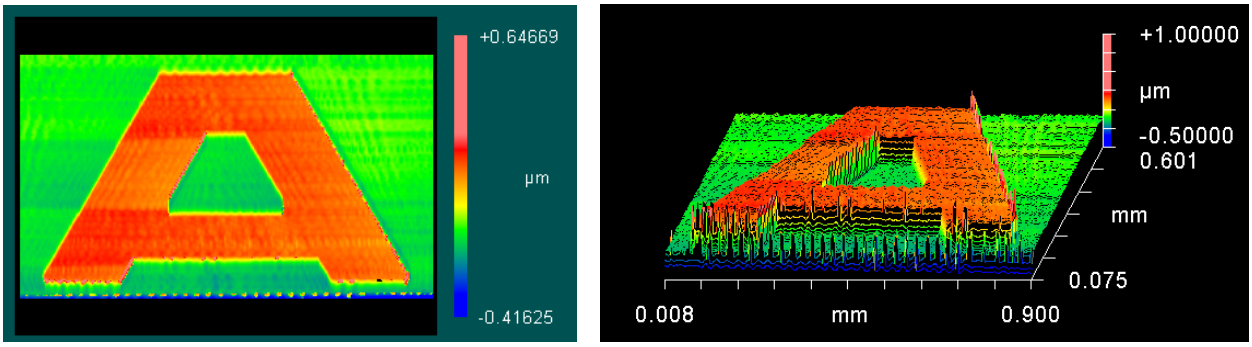

Figure 6. White light interferometer image of machined shape

REFERENCES

1. Schaller, T, Heckele, M, M. Ruprecht, R, “Mechanical Micromachining for Mold Insert Fabrication and Replication”, ASPE Proceedings, Vol.19, Pg 3-8, 1999.

2. Negishi, N, “Elliptical Vibration Assisted Machining with Single Crystal Diamond Tools”, MS Thesis, NC State University, 2003.

4 LIVE-AXIS TURNING

Nathan Buescher
Graduate Student
Alex Sohn
Precision Engineering Center Staff
Dr. Thomas A. Dow
Professor
Department of Mechanical and Aerospace Engineering

4.1 INTRODUCTION

The objective of the development of a Live-Axis Turning (LAT) Axis is to apply recent advances in air-bearing slide design and linear motors to increase the velocity and range of tool motion and demonstrate a commercially viable device that will extend the fabrication capability of non-rotationally symmetric (NRS) surfaces. This technology, aided by high-resolution feedback devices and advanced control algorithms, will allow NRS surfaces to be machined efficiently and accurately on currently available diamond turning lathes. The goal is to create a tool axis capable of 4 mm displacement at 20 Hz.

Diamond turning has revolutionized optical fabrication because of its ability to accurately and rapidly create optical surfaces as well as opto-mechanical features used in optical alignment. An emerging trend in optical design is the use of optical surfaces that are not rotationally symmetric (NRS). When such surfaces are included in an optical system, the complexity, bulk and weight of the system can be reduced. The shape of these surfaces can typically be divided into a best-fit sphere or asphere and a non-symmetric component as illustrated in Figure 1. It is this non-symmetric component of a surface that required the use of a fast axis.

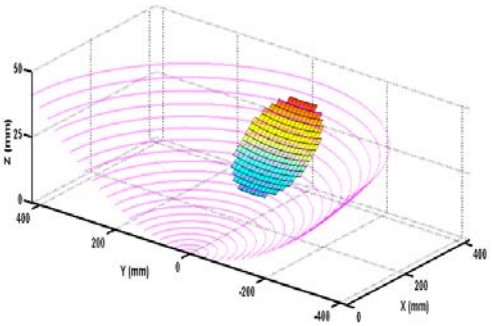

a.) Off-axis toroidal mirror

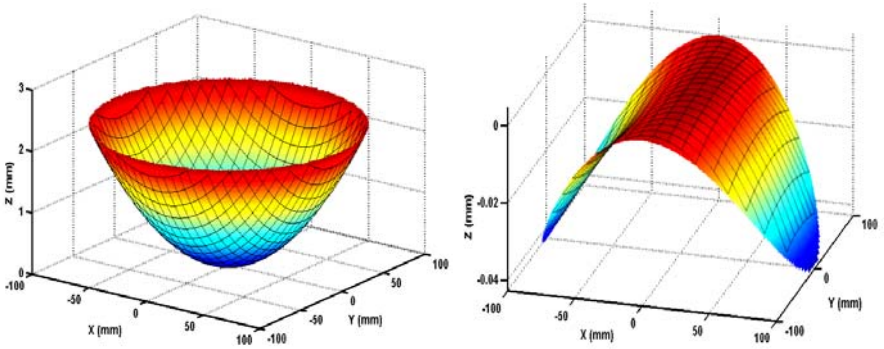

b.) rotationally symmetric component of mirror c.) NRS component of the mirror

Figure 1. Decomposition of mirror surface (a) into symmetric (b) and non-symmetric (c) components for on-axis fabrication.

NRS surfaces can be created on a Diamond Turning Machine (DTM) by using two standard axes (slow) to generate the entire surface or three standard axes with a fly cutter to raster scan the surface. Problems arise with these two methods: in the first method the spindle speed must be less than 50 rpm because of the low bandwidth of the standard (slow) axes and thus the time for one pass of the tool for a 25 mm part will be over one hour. The second method requires exceedingly slow scans to produce an optical surface finish with a flycutter. Thus, long machining times and the associated thermal drift hamper both methods. Another technique is to add a Fast Tool Servo that is synchronized to the rotary position of the spindle on a 2D lathe. This arrangement will make a diamond turning machine more versatile and can efficiently produce an NRS optical surface. The main axes of the DTM create the symmetric component, the FTS adds the non-symmetric component and together they create the desired optical shape. The range of this auxiliary FTS axis dictates the maximum feature size possible while the feed rate and spindle speed have a direct bearing on the time to fabricate the surface and the cost. The new LAT Axis exceeds the range of the commercial FTS by a factor of 10 while the operating frequency is more than 25 times greater than when using the machine slides.

4.2 ACTUATOR DESIGN

The goal is to develop a lightweight, high-speed, air bearing, linear motor driven slide that can operate with a stroke of 4 mm at 20 Hz. The LAT Axis design consists of a lightweight aluminum-honeycomb slide driven by a linear motor and guided by stiff air bearings. A holder for a diamond tool is attached to the front of the slide. A drawing of the proposed LAT system is shown in Figure 2.

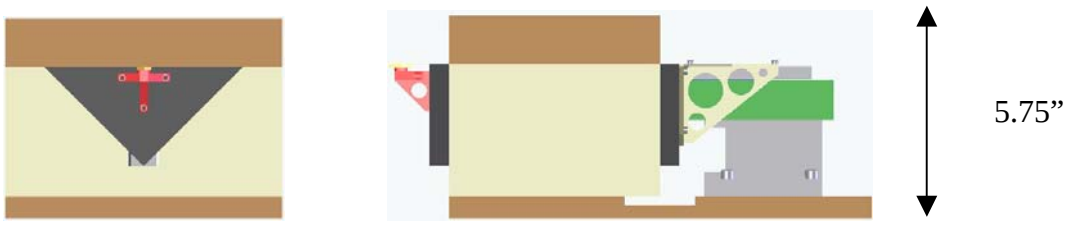

Figure 2. Front view (left) and side view of Live-Axis Turning Axis

Slide Material The first step in the axis design was to select a material for the slide and develop the shape of the cross-section. The slide require a small moving mass, high stiffness to produce a high natural frequency for the system and sufficient surface area to produce a stiff air bearing. For these reasons, aluminum honeycomb was selected as the working material. Aluminum honeycomb consists of a honeycomb core of fine aluminum sandwiched between two thicker aluminum faces. The core cell structure holds the face sheets apart to generate the high bending stiffness but its low shear strength tends to decrease the theoretical stiffness by about 80%. The properties of flat honeycomb samples were calculated and measured, and a model for the actual material properties (modulus, density) was constructed. This model was used in the analysis discussed next.

4.3 FEM ANALYSIS

To help select an optimum cross-section shape, finite element models were created for different candidate shapes. Three basic shapes were analyzed: a box, a V-shape, and a triangle as illustrated in Figure 3. The properties of interest are the bending stiffness, mass, first natural frequency, center of gravity, location of the linear motor and location of the position sensing encoder.

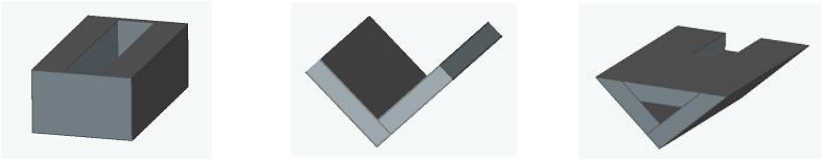

Figure 3. From left to right, the box, V-shape, and triangular slide designs

After simulating bending and frequency analysis tests for each slide shape, the box design was eliminated because removal of material to embed the motor caused a large drop in natural frequency. The remaining designs were compared using data obtained from simulations and shown in Table 1.

Table 1. Comparison of V Shape and Triangle slide designs

	Mass (g)	Nat.Freq. (Hz)	Lateral stiffen ss (N/μm)	Vertical stiffness (N/mm)	# Parts
V Shape	400	3450	8.145	8.17	4
Triangle	445	3950	25	10.5	2

Although slightly heavier, the triangle cross-section was selected because it proved more resistant to static forces resembling tool-tip loads, displayed a higher natural frequency than the V shape and included a housing structure with few parts, simplifying the assembly process.

4.3.1 SLIDE LENGTH

Another important design issue is the length of the moving slide. As the slide length increases, the bearing stiffness and natural frequency increase due to the larger surface area. However, the structural natural frequency of the moving slide decreases as the length increases. After analyzing the changes in natural frequency and the rate of change of stiffness with bearing length, a 7" slide was selected as the optimum length.

4.3.2 MOTOR SELECTION

A brushless linear motor was chosen for its smooth motion characteristics, high accuracy, repeatability, high acceleration capabilities and stiffness. To reduce the moving mass of the system, the smallest/lightest motor capable of producing enough continuous force to drive the system was desired. Equation (1) was used to determine the force needed to drive the system:

$$F = mA\omega^2 \tag{1}$$

where m is the mass in Kg, A is the amplitude in m and ω is the frequency in Hz. For an assumed moving mass of 500 g, an operating frequency of 20 Hz , and amplitude of 2 mm (for a total stroke of 4 mm), 15.8 N are needed to drive the system. From the Airex Linear Motor P12 Series, the P12-1 is chosen (continuous force 27 N [2]). This motor weighs 100 g.

4.3.3 MOUNT BRACKET

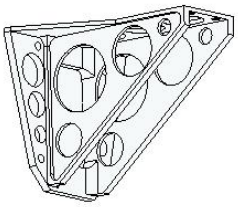

Figure 4. Improved final bracket

The motor mount bracket connects the motor to the slide. The bracket must support the full weight of the motor, provide a rigid coupling to the slide and have minimum weight. The first bracket tested had a square faceplate to be bolted to the rear of the slide and a channel with 1/16" thick walls and vertical gussets to contain the motor as illustrated in Figure 4. However, this bracket was disappointingly flexible allowing the motor and slide too much deflection. As a result of modeling, the faceplate was made taller to provide more resistance against vertical bending and horizontal gussets were added. Lightweighting holes were also added to the bracket in non-critical locations to reduce the mass.

The new bracket performed well in dynamic simulations. The natural frequency of the slide-bracket-motor system was increased by nearly 50% and deformation was reduced to magnitudes seen in the slide and motor, indicating sufficient stiffness.

4.3.4 EXPERIMENTAL VERIFICATION

When the moving slide was fabricated, accelerometers were used to observe its dynamic characteristics and compare those results to the predicted behavior. A free-free natural frequency test was used both with and without the motor and bracket. The setup for the experiment is shown in Figure 5.

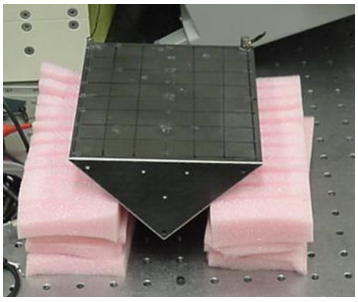

Figure 5. Setup for frequency analysis

A hammer was used to strike the slide resting on soft foam. The attached accelerometer then reported the vibration. The results are given below in Table 2.

Table 2. Experimental results for natural frequency test (moving slide only)

	1st Natural Frequency (Hz)	2nd Natural Frequency (Hz)	Ratio of First/Second
Predicted Results	3950	5110	0.77
Actual Results	3540	4660	0.76

With the values for the first and second natural frequencies showing a near match, two accelerometers were used to observe the vibration at different spots simultaneously on the slide. The relative magnitude and phase data of the two positions confirmed the predicted mode shapes: a twisting motion at the first frequency and a bending mode at the second.

4.4 CONTROL SYSTEM DEVELOPMENT

A linear motor depends on a control system to provide both static and dynamic stability. The following error, stiffness, disturbance rejection and stability depend on the drive system, the moving mass, the feedback sensor, the controller algorithm and update time. The control system must have fast loop update time, be flexible enough to support different control strategies and have the appropriate input/output configuration to support the required hardware. In this application, a straightforward proportional, integral, derivative (PID) control scheme may not be sufficient [3]. Feedforward gains will be investigated to eliminate following error. The UMAC controller from Delta Tau Systems is used to implement axis control.

4.5 MACHINING EXPERIMENTS

The goal will be to create optical surfaces that can be measured to evaluate the quality of the machining process. Two types of surfaces will be created. The first will be a tilted flat. For this type of surface, the LAT axis moves one cycle per revolution in a sine wave motion that linearly increases with radius. Because the resulting surface is flat, it can be easily measured using interferometers and profilometers to quantify the figure error and the surface finish. The second surface to be created will be a more complex NRS surface. Each of these surfaces will be used to test the capability of the LAT process to generate complex surfaces.

4.6 CONCLUSIONS AND FUTURE WORK

The 7” long slide for the Live-Axis Turning system will be made of aluminum honeycomb and have a triangular cross section with faceplates at the front and back. The rear faceplate of the slide will have a relieved area to accommodate the magnet track of the motor used to drive the system, which is an Airex P12-1 brushless linear motor. A linear scale encoder will be mounted on the flat top of the piston to provide position feedback to the controller.

Future work to be completed on this project includes:

1. Assembling the LAT system and aligning the tool height on the Nanoform diamond turning machine. This process includes the design of a spacing block and a flexure to allow for small tool height adjustments.
2. Integrating the LAT system with the controller and adjusting gains to achieve optimal system performance. A Delta Tau Turbo UMAC will be used to command the LAT axis motor as well as gather position feedback from the piston's encoder.
3. Conducting machining experiments to assess the LAT performance. One such experiment will be to machine a tilted flat. Small changes may be made to improve the system performance, and the results will be detailed in a full report.

REFERENCES

1. Garrard, K., A. Sohn, R. G. Ohl, R. Mink, V. J. Chambers. "Off-Axis Biconic Mirror Fabrication." *Proceedings from the EUSPEN 2002 Annual Meeting* (2002).

2. Airex Corporation. Dover, New Hampshire, http://www.airex.com

3. Lin, C. L. "Multiobjective PID Control for a Brushless Linear Motor: An Evolutionary Approach." *IEE Proceedings Electric Power Applications*, v 149, No. 6, Nov 2002, p. 397-406.

5 NON-CONTACT TRANSPORTATION USING FLEXURAL ULTRASONIC WAVE

Yin Yanbo
Graduate Student
Paul I.Ro
Professor
Department of Mechanical & Aerospace Engineering

5.1 INTRODUCTION

In manufacturing and processing precision products such as compact discs, LCD, LSI and silicon wafers of semiconductors, a non-contact transportation system is indispensable to eliminate tiny defects and scratches. In order to realize such a system, several techniques have been proposed, e.g. gas bearing: transportation with an electromagnetic force or a static electronic force. In these systems, however, several problems must be overcome: (1) Levitated objects are constrained to electrically conductive materials except the gas bearing. (2) In the gas bearing systems, not only an abundance of gas is needed, but also the levitation and transportation mechanism is too complicated and expensive to be conducted. Acoustic levitation can be employed in a non-contact transportation system due to the following advantages: (1) no materials type limited to the levitated object, (2) compact size, (3) free of noise and (4) no demand on large amount of clean gas. This project conducted in PEC first investigated acoustic levitation, designed the experiment setup, proposed governing equations of acoustic levitation and checked the validity. In this report, the experiment setup for the transportation system is described.

5.2 DETAILS OF THE PROJECT

5.2.1 NEAR FIELD ACOUSTIC LEVITATION (NFAL)

The relationship between levitation and input voltage is shown in Figure 1 where it can be seen that the levitation distance is proportional to the amplitude. The top two lines represent the levitation of two objects with different mass but same mass area ratio.

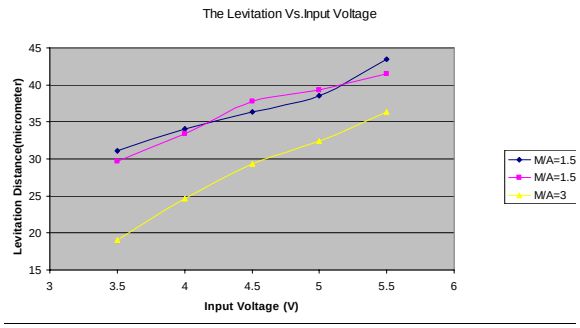

Figure 1. Levitation vs. Input Voltage

Experiment Set-up

The experiment was carried out using the configuration shown in Fig 2. It consists of one rectangular vibration plate (54*40*3 mm) and one mechanical horn connected to the Piezo actuator. The actuator was Bolted Langevin type Transducer (BLT) manufactured by NTK (Model No. DA2228). The levitated object was placed on the surface of the rectangular plate which was excited at frequency of 16.8 kHz. The vibration amplitude measurement was conducted by a Capacitance Gage and the levitation distance by laser displacement meter (Angstrom Resolver Model 101), respectively. Aluminum was chosen as the material of horn and beam because of its excellent acoustic characteristics.

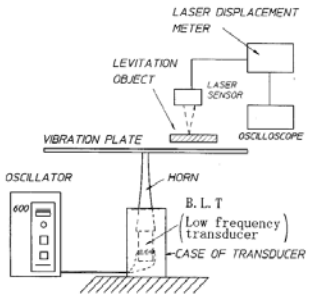

Figure 2. Experimental Set-up

Amplitude distribution on the plate Fig 3 shows the distribution of amplitude on the vibration plate. Fig 4(a) is the Chladni's pattern of vibration and (b) is the mode shape simulated by Ansys. The dissymmetry of the pattern in Fig4 (a) may arise from bad horizontality of the plate.

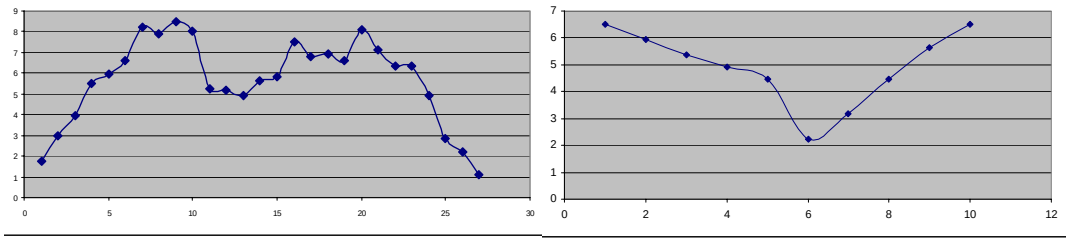

(a) Longitude Distribution of Amplitude (b) Sectional Distribution of Amplitude.

Figure 3. Amplitude Distribution on the plate

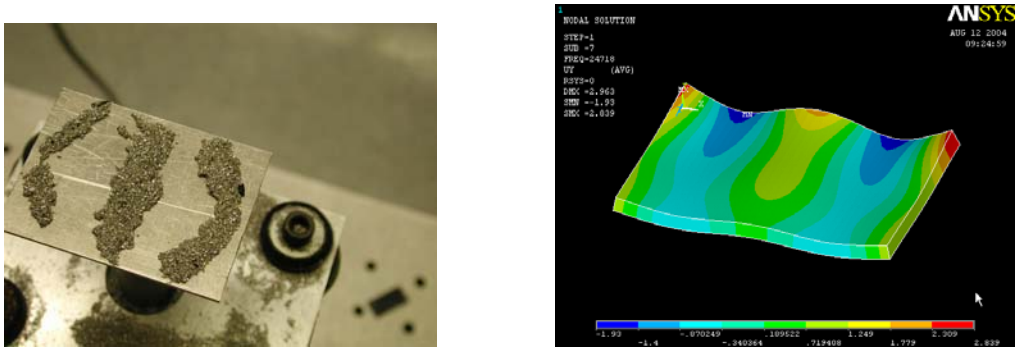

(a) The Chladni's pattern of vibration mode (b) Mode shape of vibrating plate

Figure 4. Amplitude Distribution and Mode Shape

Analytical Approach

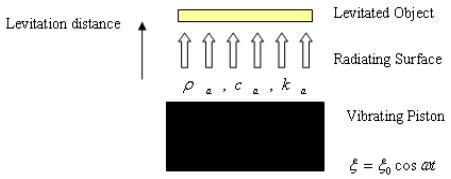

Figure 5. Levitation by Piston Vibration

Levitation by piston vibration Consider an object with planar bottom levitated by an acoustic standing wave, which is radiated from a piston-like sound source, as shown in Figure 5. The surface of levitated object is assumed to be rigid plane, and the piston vibrates as $\xi = \xi_0 \cos \omega t$.

Based on formation derived by B.Chu and R.E.Apfel [2], when levitation distance l is small enough to satisfy $k_a l << 1$, the radiation pressure is

$$P = \frac{1+\gamma}{4} \rho_0 c^2 \frac{\xi_0^{\ 2}}{l^2} \tag{1}$$

Each symbol is defined below:

P- Radiation pressure, $K = \frac{1+\gamma}{2}$, γ -specific heat ratio (for air $\gamma = 1.4$), $k_a = \omega / c$, *c*-sound velocity, l - Levitation distance, ξ_0 - Vibration amplitude, ρ_0 - Medium density.

Then levitation distance can be derived by making *W* equal to *P* as below:

$$H = c\xi_0 \sqrt{\frac{\rho_0 K}{2W}} \tag{2}$$

where:
W weight = area of levitated object.

Levitation by flexural vibration Consider that a plate vibrates in the flexural mode and a planar object is levitated by a distance of h as shown in Figure 6. In this case, the acoustic wave does not propagate normal to vibrating source. The particle velocity amplitude distribution can be derived as the sum of plane waves [3]:

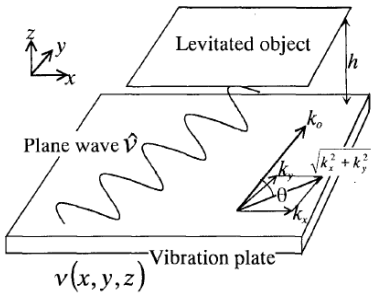

Figure 6. Scheme of Levitation by flexural vibration

$$v(x, y, z) = \frac{1}{4\pi^2} \iint \hat{v}(k_x, k_y) \times \exp[\, j(k_x x + k_y y + k_z z)] dk_x dk_y \tag{3}$$

Where:

$$k_x^2 + k_y^2 + k_z^2 = k_a^2 = (\omega / c)^2 \tag{4}$$

For a plane wave, it has two wave vectors: k_x, k_y, the radiation pressure in the z direction is derived as:

$$P(k_x, k_y) = \frac{1+\gamma}{2}[1 + \frac{\sin(2k_z h)}{2k_z h}] < E_z(k_x, k_y) > \quad (5)$$

Where:

$$< E_z(k_x, k_y) >= \frac{\rho_a \hat{v}^2(k_x, k_y)}{4\sin^2 k_z h} \quad (6)$$

The total radiation pressure in z direction can be the sum of each vector component and given as:

$$P\big|_{z=h} = \iint\limits_{k_x^2+k_y^2<k_a^2} P(k_x, k_y) dk_x dk_y \quad (7)$$

5.2.2 ULTRASONIC TRANSPORTATION

Figure 7 shows the schematic diagram of the non-contact transportation system using flexural traveling wave. The traveling wave sound source produces two unidirectional forces on the object in the gap. One is in the normal direction and levitates the object and the other induces the near boundary streaming in the parallel direction. The velocity gradient of the near boundary streaming on the surface of the object produces the viscous force that causes the object to move in horizontal direction.

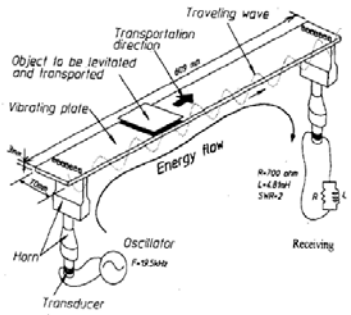

Figure 7. Scheme of Transportation System

When the beam starts to vibrate, the plate is rapidly levitated and gradually accelerated along the wave propagation direction by the viscous force [3]. The exact governing equation that describes the air velocity gradient and the effect on the transport speed of object has not been conducted out yet.

Mechanical Horn Design

The vibrating motion generated by the actuator is normally too low for practical use, so it is necessary to magnify this motion, which is the function of a mechanical horn (also called amplitude transformer) that acts as a resonant element in the compression mode. Figure 8 is one horn combined with step and exponential horn, which is being incorporated in the research.

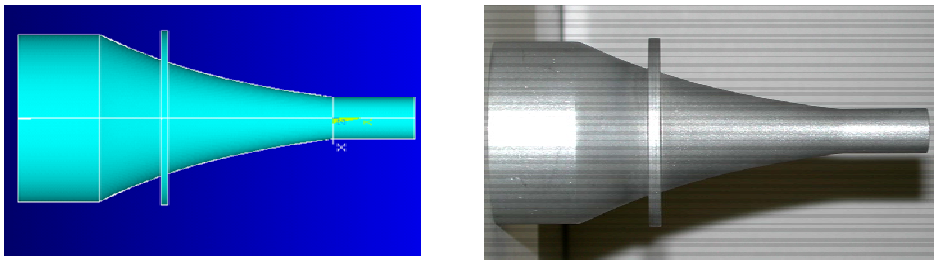

Figure 8. Combined Horn

Beam Design

It is simple to design the beam, but it is of great importance to determine position of the actuator attached to the beam, because that determines the scale of vibration velocity. Normally, the horn is attached to the beam at a length of $\lambda/4$ from the end.
Figure 9 and Figure 10 show the beam mode shape of beam.

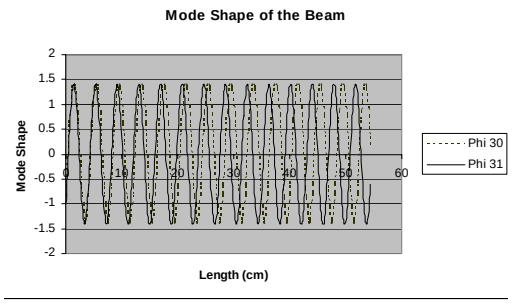

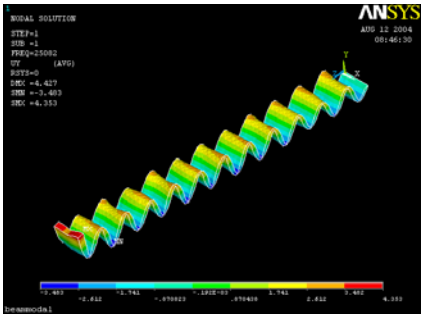

Figure 9. Mode Shape of 30th and 31st

Figure 10. Modal Simulation using Ansys

Beam and Horn Combination Analysis

When the horn is attached to the beam, the natural frequency of the horn will change. The modal and harmonic analyses are undertaken by incorporating beam and horn into one part. Figure 11 is

the modal analysis and Figure 12 the harmonic analysis, respectively. It can be seen that in the frequency of 28 KHz, the beam and horn will have the maximum vibration amplitude.

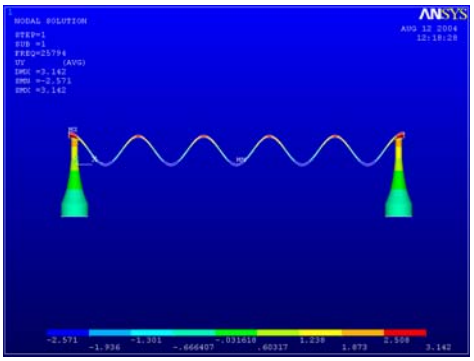

Figure 11. Modal Analysis

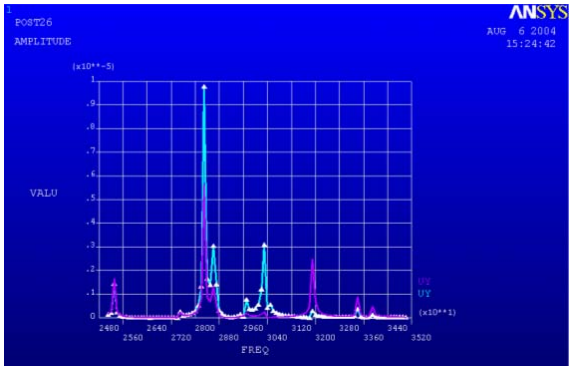

Figure 12. Harmonic Analysis of beam and horn

5.3 CONCLUSIONS

It is concluded that NFAL can be achieved with flexural wave resource. The levitation distance is proportional to the vibration amplitude. It is helpful to incorporate beam and horn into one during the experiment setup. The non-contact transportation system can be devised based on NFAL and viscous force. The future work would be (1) Experimental setup and analytical approach; (2)Ansys analysis of system and simulation on air radiation;(3)Control of object transportation

REFERENCES

1. Hideyuki Nomura, Tomoo Kamakura and Kazuhisha Matsuda, ”Theoretical and experimental examination of near-field acoustic levitation,” J.Acoust.Soc.Am. 111(4),1578-1583,(2002).

2. Boa-The Chu and Robert E. Apfel, “Acoustic radiation produced by a beam of sound,” J.Acoust.Soc.Am.72(6), 1673-1687, (1982)

3. Sadayuki Ueha, Yoshiki Hashimoto and Yoshikazu Koike,”Non-contact transportation using near-field acoustic levitation ,” Ultrasonics 38 ,26-32,(2000).

4. Yoshikau Koike,Sadayuki Ueha,Atsushi Okonogi, Takafumi Amano and Kentaro Nakamura,"Suspension Mechanism in Near field acoustic levitation phenomenon," IEEE ULTRASONICS SYMPOSIUM,671-674,(2000)

5. Yoshiki Hashimoto, Yoshikazu Koike and Sadayuki Ueha, "Near-field acoustic levitation of planar specimens using flexural vibration," J.Acoust.Soc.Am.100(4),2057-2061,(1996).

6. Lin Zhongmao, *The Principle and Design of Ultrasonic Amplitude Transformer*,Science Press,Beijing,1987.[In Chinese].

6 FAST TOOL SERVO PERFORMANCE

Anthony Wong
Undergraduate Student
Witoon Panusittikorn
Post Doc Researcher, Precision Engineering Center
Thomas Dow
Professor
Department of Mechanical and Aerospace Engineering

6.1 INTRODUCTION

The fabrication of Non-Rotationally Symmetric (NRS) surfaces cam be performed with a high-speed axis to move the tool as function of the spindle rotation. This has normally been a piezoelectric driven tool holder know as a Fast Tool Servo (FTS). Such devices have been available for over 20 years since Lawrence Livermore Labs created a design to correct spindle errors on the famous Large Optics Diamond Turning Machine (LODTM). However, these devices have only recently become widely accepted and applied to precision fabrication processes in industry. There are a number of reasons for the delay including reliable sources of FTS hardware, fast/robust controllers and software to create the desired tool path. More recently, non-linear performance associated with the control of these servos has received attention. Specifically, the change in the transfer function between the input voltage signal and the output motion of the servo as a function of the amplitude and frequency of the commands has become an issue. As described in Section 2 of this report and in Section 11 of the 2003 Annual Report [1], one of the research projects at the PEC is the development of an inverse deconvolution algorithm to reduce the magnitude of the error created by the FTS dynamics. One of the prerequisite pieces of information for this algorithm is the shape and repeatability of the transfer function of the fast tool servo (FTS).

The Variform FTS has been used by a variety of precision manufacturing enterprises to create NRS optical surfaces. This device is driven by a pair of piezoelectric actuators with a t-shaped lever to increase the range to 400 μm. The FTS has a built-in analog control system that uses an LVDT for position feedback to control the dynamics of the mechanical system. Unfortunately, this LVDT has its own dynamics. Thus, to find the transfer function of the Variform, an external sensor, rather than the LVDT, must be used to measure the actual motion of the tool. By measuring the transfer function with the LVDT and again with the external sensor, both the motion of the tool and the apparent motion from the LVDT can be determined. The shape and repeatability of each transfer function is the goal of this project.

6.2 DETAILS OF THE PROJECT

To develop a technique to characterize the dynamics of the Variform, two measurements are needed: 1) the shape and repeatability of the transfer function between the input command to the Variform and the resulting tool motion with an external sensor (laser interferometer), and 2) the shape and repeatability of the transfer function between the input voltage to the Variform and the LVDT output from the Variform controller. Figure 1 shows the relationship between the components of the system. If the first transfer function (LVDT out/Input) divided by the second transfer function (Laser out/Input) is constant; that is, independent of command amplitude and manufacturing variations between specific examples of the FTS, inverse dynamics can be programmed based on the LVDT calibration of each device. This would discount the need for an external measurement system to calibrate the FTS performance. If, on the other hand, the relationship between LVDT out and Laser out was different for each Variform, an external sensor will be needed.

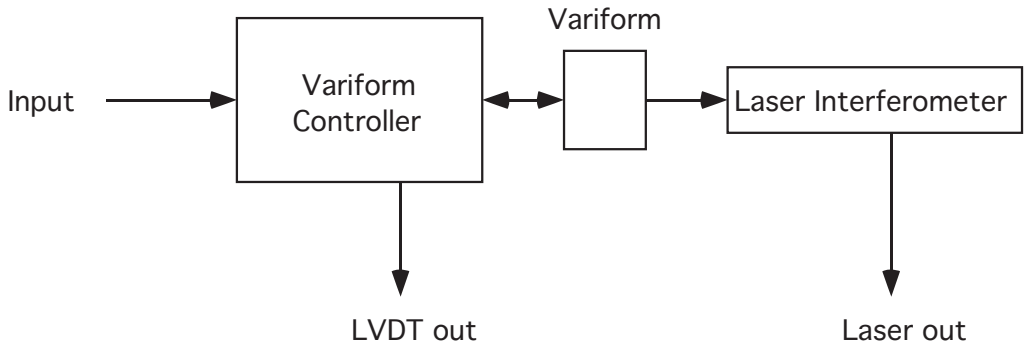

Figure 1. Measurement of the Variform Dynamics

One way to determine the transfer function of a system is to excite the system with a sine wave of a given frequency. The excitation signal is then compared with the response signal to determine the gain and phase of the system. However, this method only gives the frequency response for one frequency, so the process needs to be repeated at other frequencies to obtain the transfer function over the range of frequencies of interest. One solution to automate this method is to use a swept sine wave with discrete changes in frequency. This swept sine wave runs at one frequency for a certain number of cycles and then increases in frequency and runs at the next frequency and so on. The swept sine wave input can be broken up into bands, each with a constant frequency content, and compared with the output response to get the transfer function of the system in a range of frequencies. This method was used to find the system dynamics of both the LVDT and the Variform.

6.2.1 LVDT OUT/LASER OUT

To isolate the dynamics of the LVDT system in the Variform, the tool motion was measured with a displacement sensor external to the device. The selection of a sensor was difficult because of the large range of motion and the high-speed of the Variform. Some preliminary experiments were done with a capacitance gage but the range of motion was less than 100 µm. To provide both long-range and high-speed capability, a Zygo Axiom distance measuring laser interferometer was chosen. This device has a range of 5 m and a velocity limit of 1.8 m/sec. Because the interferometer was used to measure the position of a tool, a normal retroreflector could not be mounted on the tool because of its size. For this application, a single pass setup shown in Figure 2 was used.

The single pass includes a lens on the output of the beam splitter to bend the measurement beam so when it bounces off a small mirror mounted on the face of the tool shank, it has the proper spacing to recombine with the reference beam. Because this is a focusing system, it has a limited range - approximately 1 mm – but that was sufficient for these measurements. Two quarter-wave plates are also added to this configuration to change the polarization of the beams as they pass through them. The solid line in Figure 2 is vertically polarized and it will pass through the polarizing beam splitter unchanged but after traversing through the quarter-wave plate twice, it will be horizontally polarized and reflect into the detector. The dotted horizontal beam will do the opposite, that is, reflect the first time and then pass through to the detector the second time.

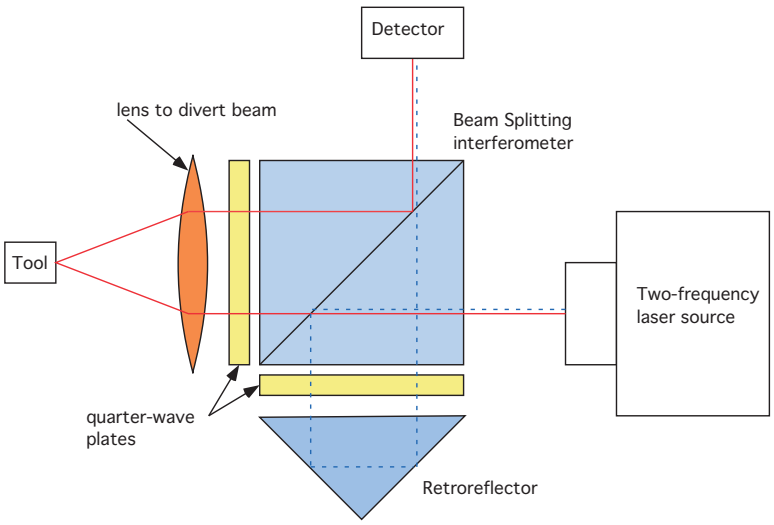

Figure 2. Interferometer used to measure the Variform motion

The Axiom laser interferometer produces a digital word that describes the position of the target at very high speed – update rate is 250 MHz. A dSPACE data acquisition board (RS1104) was

used to convert the digital output of the laser to an analog voltage. A spectrum analyzer (Stanford SR780) was used to generate the swept sine wave as well as to calculate the transfer function. The dSPACE board also inverts the excitation signal to create the differential signal necessary for the Variform amplifier.

The output of the laser measurement of position and the LVDT output from the Variform were compared to find the transfer function of the LVDT out/Laser out. The results of these experiments are shown in Figure 3. Unfortunately, this transfer function is not the same for all Variforms. After comparing two Variforms, it was found that the LVDT/Laser dynamics had the same shape, but the magnitude of the first Variform must be shifted to match the gain of the second. Figure 3 shows the magnitude of the LVDT/Laser for the Variforms # 0113 and # 0144. After the magnitude of # 0113 is shifted up by .71 dB, the magnitudes of the LVDT dynamics of the two Variforms match up very well. Figure 3 also shows the phase of the LVDT dynamics, which are the same for both actuators. If the gain issue is ignored, the LVDT dynamics were determined to be a function of the excitation frequency but independent of the amplitude of excitation.

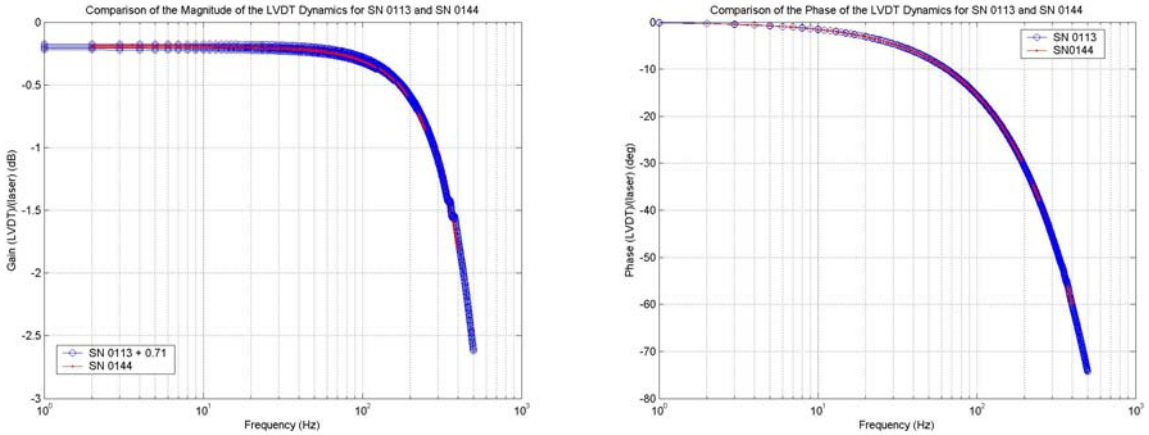

Figure 3. Comparison of the Magnitude and Phase of the LVDT/Laser Dynamics

6.2.2 LVDT OUT DYNAMICS

The second part of the project was to develop an automated procedure using LabView software and a National Instruments data acquisition board to generate the transfer function between the input to the Variform and the LVDT output from the Variform controller. This system could be used to calibrate FTS performance as a function of operating time or after repair.

Repeatabilty The LabVIEW frequency response results are repeatable. Figure 4 shows the standard deviation among 10 trials each of sweep sine waves from 0 to 500 Hz at voltages from 1 volt up the maximum of 10 volts. Because of the limits of the Variform operation, some of the

higher amplitudes were stopped well below 500 Hz. The data shows the maximum standard deviation in magnitude is 0.09 dB and in phase is 0.5 degrees. The standard deviation of the results increases with decreasing amplitude meaning that the noise is somewhat fixed and has more impact on the lower amplitude voltages. .

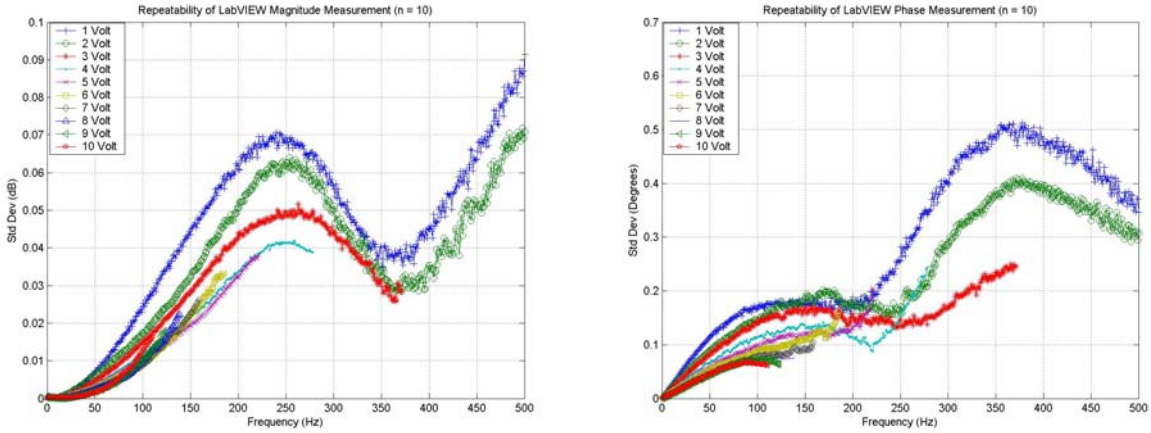

Figure 4. Repeatability of Magnitue and Phase Measurement

Output Noise The LabVIEW output voltage is close to the actual voltage commanded. The output voltage noise is less than 80 millivolts.

6.3 CONCLUSIONS

The measurement of different examples of Variform FTSs indicated that the shape of the transfer function between the LVDT out and the Laser out was a function of frequency but not of the amplitude of the excitation voltage. However, there were differences in gain for the two examples studied. A calibration system was developed to measure the relationship between the input voltage to the Variform and the LVDT reading that uses LabView software and a data acquisition board from National Instruments. A convenient user interface has been developed and used to assess the repeatability and noise during the swept sine measurements. The data for 10 repeated tests indicated that the amplitude repeatability is better than 0.1 dB and the phase deviation is less than 0.5 degrees.

7 MICROELECTRONIC COOLING USING PIEZOELECTRIC BIMORPHS

Simon Halbur
Graduate Student
Dr. Paul Ro
Professor
Department of Mechanical and Aerospace Engineering

7.1 INTRODUCTION

As more and more transistors are being put into faster processors, their heat generation goes up, which in turn results in the need for more powerful cooling systems to remove this heat. These cooling systems usually result in larger heat sinks and fans. While this is not a problem for most desktop computers, which have plenty of space, it is a limitation for portable computers whose main objective is to become smaller and lighter.

A possible solution to this problem is to replace the fan with a device that is able to produce the same amount of heat dissipation, but requires less space to do so. One such device could be a piezoelectric bimorph. It has been shown that a vibrating beam placed next to a plate will produce acoustic streaming between the plate and the beam [1]. If the plate is a heat source, the acoustic streaming would induce forced convection across the surface of the plate thereby increasing the heat dissipation from the plate [2]. A piezoelectric bimorph is one possible means of creating a vibrating beam. The cooling performance can be enhanced by introducing slots in the bimorph [3]. This project will take this one step further by looking at the heat dissipation requirements of current portable computers and the applicability of using PZT bimorphs to fulfill these requirements.

7.2 DETAILS OF THE PROJECT

7.2.1 ANALYSIS OF CURRENT COOLING SYSTEMS

In order to get an idea of the means by which heat is currently removed from portable computers, the cooling system of a DELL® Inspiron® 3800 notebook computer was analyzed. This computer runs Windows® 98 on an Intel® Celeron® processor operating at 600MHz with a core voltage of 1.6V. While this is an older notebook computer, the cooling system is relatively the same as more recent models. The differences are mainly in the arrangement and number of components. The general layout of the notebook's cooling system can be seen in Figure 1. The

system basically consists of a copper plate that sits directly over the processor. From the copper plate heat is routed through a heat pipe to the heat sink and fan, where the majority of the heat dissipation occurs.

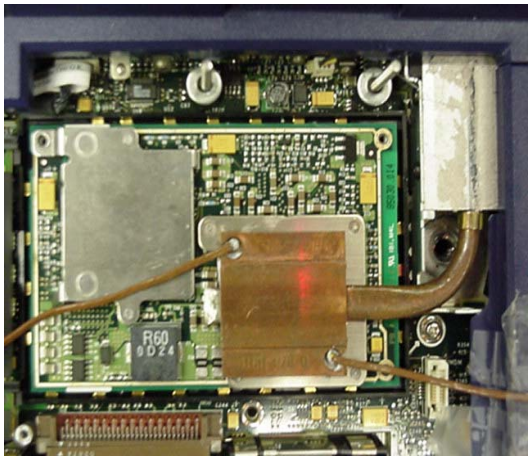

Figure 1. Computer Cooling System

Heat Transfer Analysis

In order to determine the rate of heat transfer (or heat dissipation) of the computer's existing cooling system, heat transfer analysis was performed. The analysis looked at the conductive (Equation (1)) and convective (Equation (2)) mechanisms of heat transfer [4]. Heat transfer by radiation was ignored.

$$\dot{Q} = kA\frac{\Delta T}{L} \tag{1}$$

where:

k: thermal conductivity of material
A: surface area
L: thickness of material

$$\dot{Q} = hA(T_s - T_{inf}) \tag{2}$$

where:

h: convection heat transfer coefficient
T_s: surface temperature
T_{inf}: ambient temperature

The analytical solution was verified by performing an Ansys® simulation of the computer's cooling system. The analysis looked at the steady-state rate of heat transfer.
The copper plate, heat pipe and heat sink were modeled using SOLID70 elements.
There was approx. 12% error between the Ansys® simulation and analytical model. Most of the error comes from assumptions that were made during the analysis of the heat sink.

7.2.2 COOLING CAPABILITIES OF PIEZOELECTRIC BIMORPH

Intel® provides Thermal Dissipation Power (TDP) ratings for each of the processors that it produces. This rating is the amount of power that a cooling or heat removal system must dissipate from the processor for safe operation. The TDP values are on the average of 30-35 Watts for most of the processors used in notebook computers [5]. Using previous research it was determined that acoustic streaming would not be able to produce a large enough flow velocity such that the forced convection coefficient would be able to remove this amount of power [1]. Therefore, the cooling capabilities of a bimorph were analyzed for the first and second modes of vibration in terms of the volumetric flow rate and the flow velocity that would be produced from large displacements.

Ansys® Tip Deflections

Before the volumetric flow rate and flow velocity could be obtained the bimorph's amplitude would have to be determined. Since instrumentation to measure the amplitude was not available, Ansys® simulations were performed in order to determine the dynamic tip displacement of the bimorph beams. The bimorph was modeled as a five-layer beam consisting of two piezo layers, two bonding layers and the middle shim using SOLID45 and SOLID5 elements. The element size was constrained to 0.0002 meters in order to obtain accurate results and yet limit the processing time. Harmonic analysis was then performed using a 2% damping ratio that is common for most mechanical systems.

Volumetric Flow Rate

Using beam theory, the 1^{st} and 2^{nd} modal plots, when scaled to the vibration amplitudes that were determined from Ansys®, provide the area underneath the bimorph beam. The volume displaced is then just the area multiplied by the width of the bimorph. This volume is then multiplied by the frequency of the bimorph to arrive at the volumetric flow rate. Figure 2 displays the flow rates for each of the bimorphs. The first and second modes are for bimorph free lengths of 0.06 meters whereas the two free end flow rate is for a bimorph clamped in the middle thereby creating two 0.02875 meter beams.

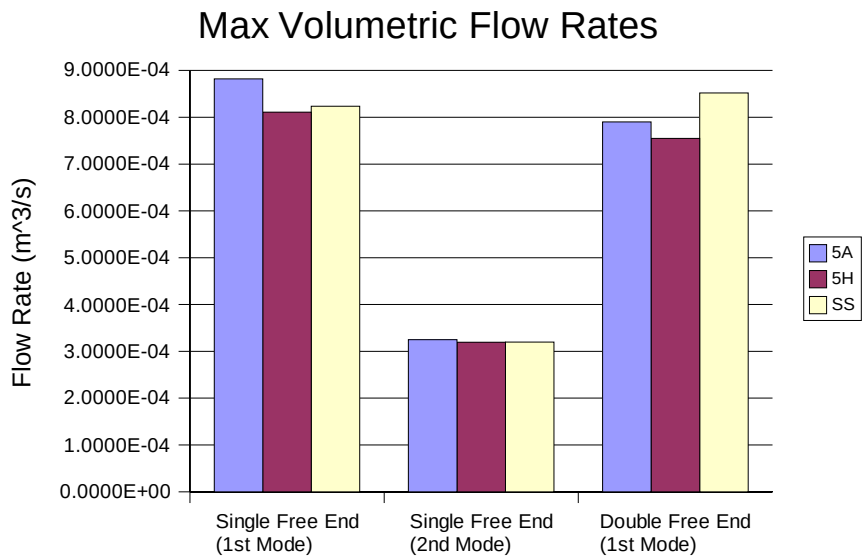

Figure 2. Bimorph Volumetric Flow Rates

Flow Velocities

Once the volumetric flow rates were determined, the flow velocities could be easily derived by dividing the flow rate by the exit area. For the first modes the exit area was taken to be the bimorph's width times its tip amplitude. The second mode exit area was taken to be twice the area derived from the modal plots. There would be one exit area for each side of the bimorph. Figure 3 displays these flow velocities.

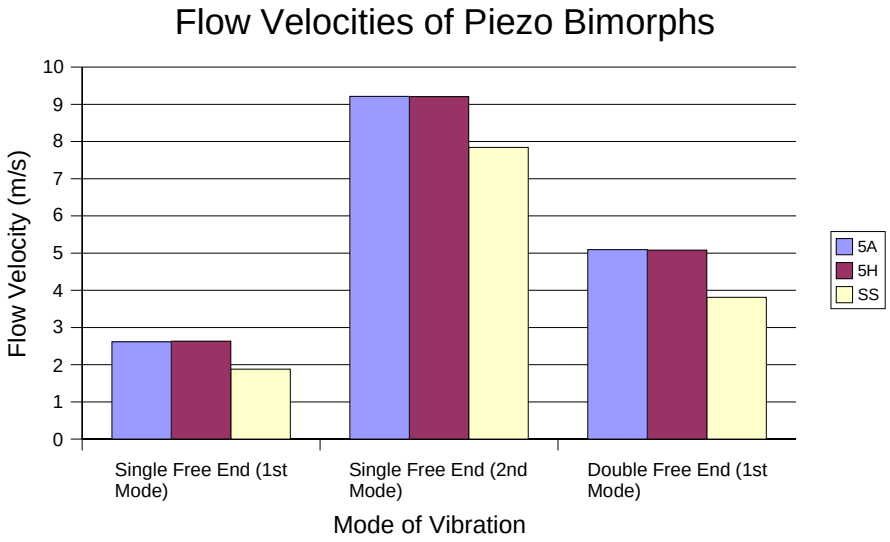

Figure 3. Bimorph Flow Velocities

7.3 CONCLUSIONS

From Figures 2 and 3, it can be seen that the first mode of vibration produces the largest volumetric rates. This can be expected because they also have the largest deflections. In terms of the flow velocities, the second mode has the highest. This is mainly due to the fact that the frequency for the second mode is the highest. When the bimorph beam was change to a shorter length, the flow velocity increased because of a higher natural frequency, but the volumetric flow rate went down because the amplitude was not as large. This is not that evident in Figure 1 because there is actually two bimorph beams so the flow rate is twice that of a single beam. The next step in the research is to look for an optimal beam length in which the flow velocity is as large as possible and yet able to move enough air to have significant cooling. Another future plan of the project is to develop an equation such that the cooling being applied by a bimorph to a heat source can be predicted by knowing all of the characteristics of the system. In other words, by using this equation it can be determined whether a bimorph would be able to cool a specific heat source.

REFERENCES

1. Nyborg, W.L., *Acoustic streaming near a boundary*, J. Acoust. Soc. Amer., vol. 30, no.4, pp 329-339, (1958).

2. Ro, P.I., and Loh, B.G., *Feasibility of using flexural waves as a cooling mechanism*, IEEE Trans. Ind. Electron., 48, pp 142-9, (2001).

3. Wu, T., Ro, P.I., Kingon, A.I., and Mulling, J.F., *Piezoelectric resonating structures for microelectronic cooling*, Smart Mater. Struct., 12, pp 181-187, (2003).

4. Çengel, Y.A., and Turner, R.H., *Fundamental of Thermal-Fluid Sciences* (New York: McGraw Hill), pp 604-814, (2001).

5. Intel®., *Mobile Intel® Celeron® Processor on .13 Micron Process and in Micro-FCPGA Package Datasheet*, (2004), http://www.intel.com/

8 METROLOGY ARTIFACT DESIGN

Karalyn F. Folkert
Graduate Student
Thomas A. Dow
Professor
Department of Mechanical and Aerospace Engineering

8.1 INTRODUCTION

Through the years, there have been a number of calibration artifacts developed including ball bars, ball and hole plates, ring gauges, and hole bars [1]. After considering these artifact standards, a ring gauge was chosen for further development. The overall features of the ring gauge (OD, ID, width and wall thickness) can be used to exercise multiple axes of a CMM. In addition, small features can be added to the ID and OD to assess the capability of the machine to deal with small temporal and spatial variations in surface features. The ring gauge can also be measured in different orientations and positions on the CMM to cover the entire working volume. Figure 1 shows the ring gauge geometry on the Diamond Turning Machine (DTM) during machining.

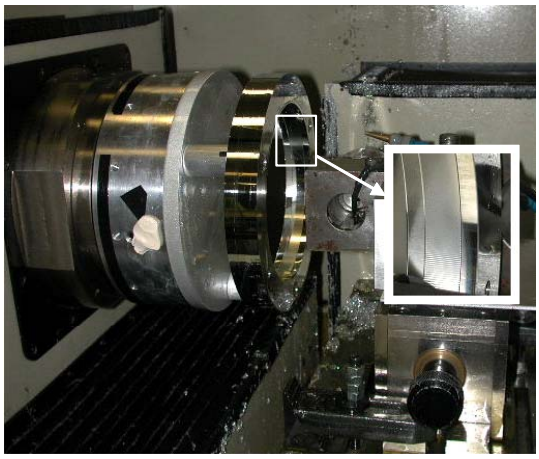

Figure 1. Ring gauge with wave feature shown in the inset.

8.2 RING GAUGE FEATURES

The first prototype of the ring gauge was created in 6061-T6 aluminum. It has a 6” (152.4mm) ID with 1” (25.4mm) square cross section and all surfaces of the gauge have been diamond turned. Reference surfaces were created on the OD and ID in the form of 0.5” (12.7 mm) wide grooves that are 30 µm deep. The OD is a smooth ring but the ID has a swept sine wave with ± 2.5 µm amplitude and spatial wavelength range from 1/80” (0.317mm) to 1/4” (6.35mm). A swept sine wave is a sine wave that continuously varies its frequency. In this case, the wave begins at the long wavelength and progresses to a short wavelength in the first 90

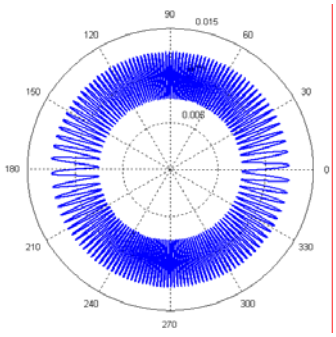

Figure 2. Swept sine wave features.

degrees. To produce a continuous wave, the wave is "flipped" to line up with the last wave and then the wavelength increases to the starting point as it reaches 180 degrees. From 180 to 360 degrees, the wave is a mirror image of the first 180 degrees. Figure 2 illustrates these features. The small surface features will assess the capability of the CMM to respond to small surface anomalies and to characterize the dynamic performance of the CMM as it traverses the varying wavelength features.

8.3 DESIGN AND FABRICATION PROCEDURE

The design of the ring was selected for a convenient size with sufficient stiffness to be usable and machinable. Significant thought went into the mounting system and machining procedure to guarantee a cylindrical shape post-machining. Figure 1 shows the ring mounted in the diamond turning machine. It is supported on a vacuum chuck with 3 one-inch diameter posts. The procedure was to machine the back of the flat vacuum plate and mount it on the spindle. The posts are installed and machined flat. The ring was bolted to the posts and the front side was machined and then flipped over and the back side is machined. Next, the ID and OD of the ring were machined. Finally, the finished reference shapes were machined: a flat cylinder on the OD and the swept sine wave on the ID.

8.3.1 FABRICATION OF SWEPT SINE WAVE

The wave features of the artifact were fabricated using a Fast Tool Servo (FTS) shown in Figure 3. An 18 mm long, hollow cylindrical piezoelectric actuator (25 mm OD and 12 mm ID) drives the device to a maximum displacement of 18 µm. A capacitance gage provides feedback on the position of the tool holder by looking at the back of it through the hollow actuator. A commanded position is turned into a positive input voltage and sent to a high voltage amplifier where it is amplified by 100 before being sent to the FTS.

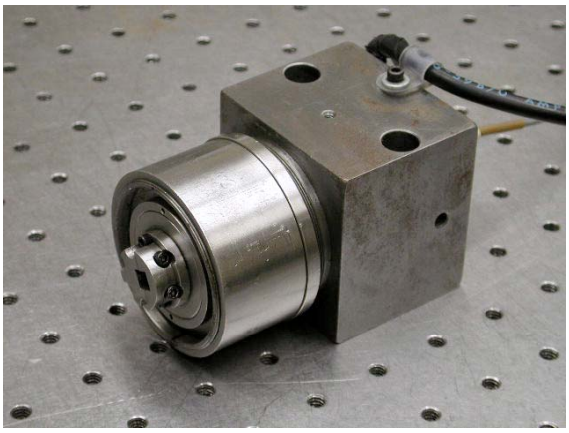

Figure 3. Fast Tool Servo.

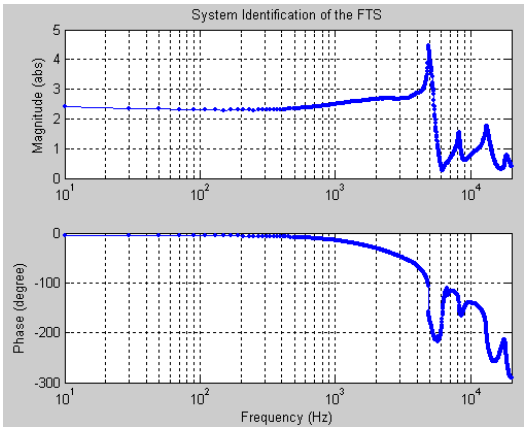

Figure 4. System dynamics of the FTS.

The open-loop dynamics of the FTS as a function of the frequency of a sine wave command is shown in Figure 4. The top graph is the amplitude ratio of the output voltage from the capacitance gage to the input voltage to the amplifier. It shows a slight decrease in amplitude with frequency up to about 400 Hz and a strong increase to the first natural frequency of 5 kHz. This frequency is a result of the first bending mode of the cylindrical plate that serves as the base for the tool holder. The phase difference between input and output shows a small offset (3˚) at DC that grows to about 27˚ at 1000 Hz.

8.3.2 First Ring Gauge Prototype

The first prototype of the ring gauge was described in the 2003 Annual Report and contained several problems including non-uniform sine wave amplitude and a distortion in the diameter of the ring. The ring was measured at Oak Ridge Y-12 facility and the results are shown in Figure 5. This prototype was machined without closed loop control of the FTS (no cap gage was installed because of space limitations). The measured sine wave features shown in Figure 5 indicate a reduction in amplitude as the wavelength approaches the smallest size (~0.3 mm). The reduction in amplitude is both at the peak and the valley of the wave. The open loop performance of the FTS (Figure 4) does not show a dramatic change in gain for the range of frequencies used (0-500 Hz). Several other explanations were evaluated to see if the cause could be identified. The ring was bolted to three stand-offs which were shown to cause some distortion when it was removed. Both of these issues must be addressed before a second prototype can be produced.

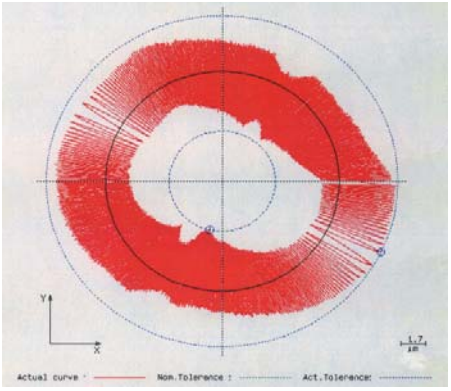

Figure 5. Measurement setup with a CMM at Y-12 and the resulting shape features.

8.4 CYLINDRICAL ARTIFACT

The next step was to determine why the swept sine wave distorted. The fabrication of the ring gauge used open loop control; so closed-loop control was evaluated to see if this was the source of the amplitude drop. To simplify the fabrication process, the sine waves were machined onto the OD of a 100 mm diameter aluminum cylinder. Figure 6 shows the setup of the experiment. The swept sine wave signal was sent to the FTS open loop, but the position of the tool was recorded by the position of the capacitance gauge.

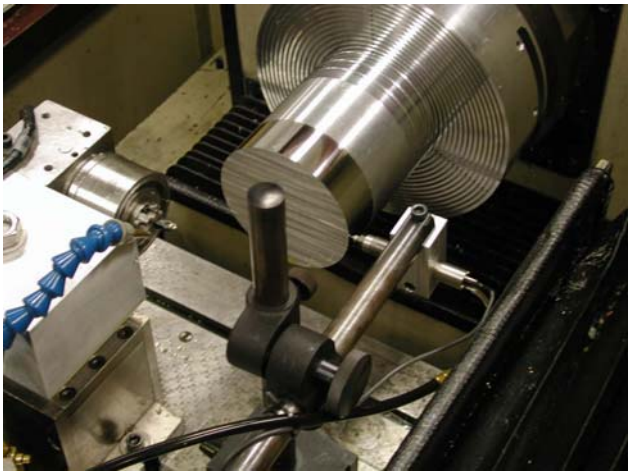

Figure 6. Experimental setup to machine swept sine wave on OD of cylinder and the air-bearing LVDT used to measure the final shape.

The cap gage output for the swept sine wave is shown in Figure 7, and it indicates an increase in voltage at the highest frequencies. This is consistent with the open loop characteristics of the FTS in Figure 4. However, a measurement of these same sine wave features shown in Figure 8 using the air-bearing LVDT exhibited the same features measured on the original ring gage; that is, reduced amplitude at the higher frequencies.

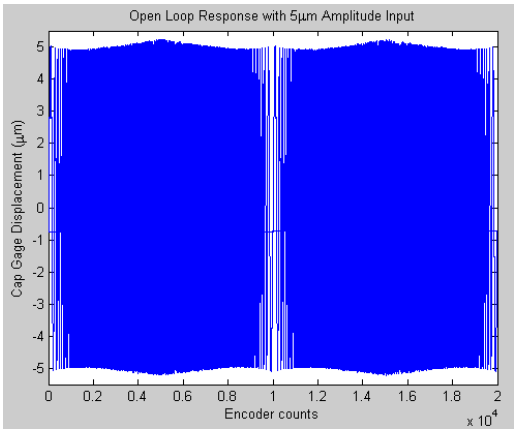

Figure 7. Cap gauge reading of 5µm input.

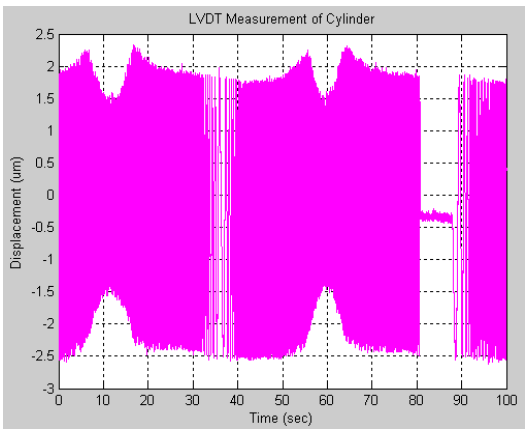

Figure 8. LVDT measurement of sine waves.

Sources of Error

The difference between the cap gauge reading and the LVDT remained a puzzle: fabrication or measurement? To address this question, several hypotheses were proposed and tested.

Tool Clearance The diamond tool on the FTS has a clearance angle of 6˚. The slope of a sine wave increases with the amplitude and the frequency. If the slope at the shortest wavelength (high frequency) is greater than the clearance angle of the tool, portions of the wave could be cut off. Equation (1) calculates the maximum slope of the swept sine wave.

$$Slope_{\max} = A * \left(2\pi / L\right) \tag{1}$$

where:

A = Amplitude of the wave (0.0025mm)

L = Minimum wavelength (0.317mm)

The maximum slope is 0.05 radian or 2.84˚ with the proposed values. On the cylinder, the shortest wavelength measured 0.186mm and 0.287mm on the ring gauge. This translates to 4.84˚ and 3.14˚, respectively. Even though the shortest wave was smaller than anticipated, the waves are not being cut off at the highest frequencies.

Probe Tip Diameter The size of the probe used for measurement may also be an issue. There is a maximum probe size that is capable of fitting into each wave. The LVDT used a 1mm diameter probe. Probe compensation equations were applied to the commanded input to determine if and where the probe would not be able to measure [2]. Figure 9 demonstrates the concept behind probe compensation.

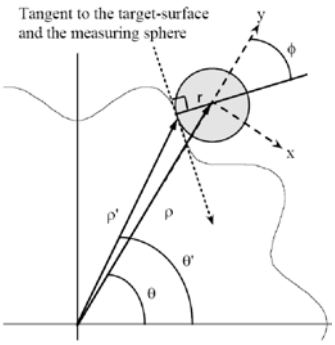

Figure 9. Probe compensation concept.

The radius is measured from the center of the part where the probe is shown on the outside surface of the cylinder. The equations of the probe compensation are shown in Equations (2-4) [2]. The probe compensation for the ID of the ring gauge would include the mean radius of the sine wave, ρ, and the radius of the probe, r, as shown in Figure 9. Figure 10 illustrates the areas where the 1mm diameter probe would not fit into the swept sine wave of the cylinder.

$$\phi = \tan^{-1}\left(-\frac{1}{\rho}\frac{d\rho}{d\theta}\right) \tag{2}$$

$$\rho' = \sqrt{\rho^2 + r^2 - 2\rho * r\cos\phi} \tag{3}$$

$$\theta' = \sin^{-1}\left(-\frac{r}{\rho}\sin(\phi)\right) + \theta \tag{4}$$

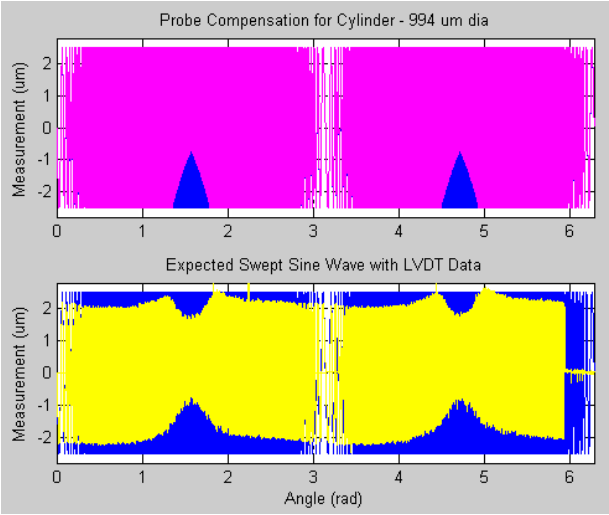

Figure 10. Top curve is the expected measurement and lower is actual LVDT measurement.

The probe compensated data showed that the LVDT probe could not measure the portions of the wave that were in the surface but indicated that the portions on the outside could be measured. This may be attributed to a shorter spatial wavelength that prevented the probe from fitting into the valley of the wave. The reduction of the peak at the shortest spatial wavelengths may be due to the filtering of the instrument if the probe lost contact with the surface after not being able to properly measure the valleys. The compensation equations do not take into account the speed of measurement and assume exact following of the wave.

8.5 CONTROL ISSUES

To develop a closed loop control system, it is important to know the open loop response of the FTS. Figure 4 shows the amplitude ratio and the phase between input and output. The first natural frequency occurs at approximately 5150 Hz. This was determined at the point where the phase reached -90°. The absolute magnitude also made a significant jump. The magnitude was determined by dividing the output voltage by the input voltage. The swept sine wave has been cut into the surface in the 10 to 500 Hz range. Even in this range, there is a change in the magnitude as well as phase. There is an initial phase lag of 3° that increases to 7°. A closed loop control system has been developed to correct for these errors.

One complication when using piezoelectric actuators is that they add hysteresis to the motion and, as a result, the gain for the system is a function of the amplitude. Figure 11 illustrates this phenomenon. The three curves are for 100%, 75% and 20% of the range of motion. Note that the P-P voltage divided by the P-P motion is not a constant: it varies from 1.846 to 1.365 at 100% and 20% respectively. This is a significant drop in gain; 25% from the full range to 20% of full range. As a result, the open-loop transfer function will change with different amplitudes of the swept sine wave. This same behavior was observed in the long range FTS (Variform) described in Section 6. Such non-linear behavior may complicate control for an arbitrary input shape.

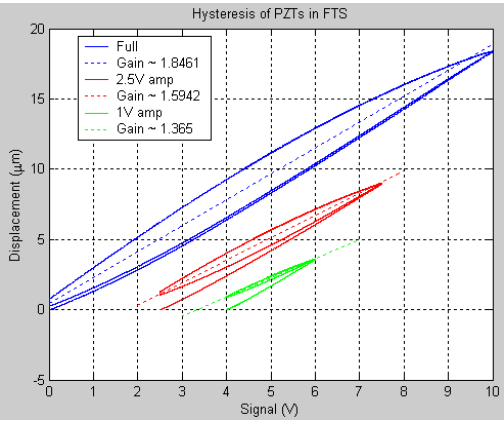

Figure 11. Hysteresis loops for different amplitudes of motion for the PZTs in the FTS.

Feedback control can correct for position error at low frequency. The closed loop control uses feedback from the capacitance gage position sensor along with proportional-integral (PI) control algorithm to correct position error. The gains were chosen based on a desired response of the system. The purpose of this closed loop control is to shape the response of the system, prevent overshoot and correct for the following error. A proportional gain of 0.3 is used to produce a constant magnitude with the chosen integral gain. The integral gain controls how quickly the system reaches its intended input. A gain of 10,000 has been chosen.

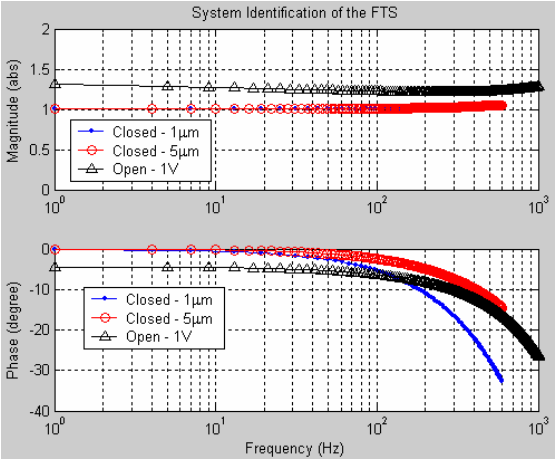

Figure 12. Comparison of closed loop and open loop system identifications up to 600 Hz.

Figure 12 shows the closed loop system response as compared to the open loop response and also demonstrates the change in the transfer function as the amplitude changes. The magnitude remains constant in the operating range of interest. There is less phase lag at low frequency but it becomes larger than the open loop value for frequencies greater than 70 Hz for the 1µm input. However, for the desired amplitude of 5µm, the phase and magnitude are always better than the open loop system.

If the swept sine wave were machined using this closed loop control system, the phase in the higher frequency waves would still put them out of place by 15˚. To reduce the effect of the FTS phase lag, the phase will be corrected using deconvolution [3]. This technique uses the closed loop dynamics of the FTS to determine a modified input signal. When the modified signal is applied to the FTS, the motion of the tool will be the desired shape. A sample swept sine wave has been fabricated on the outside of the aluminum cylinder to

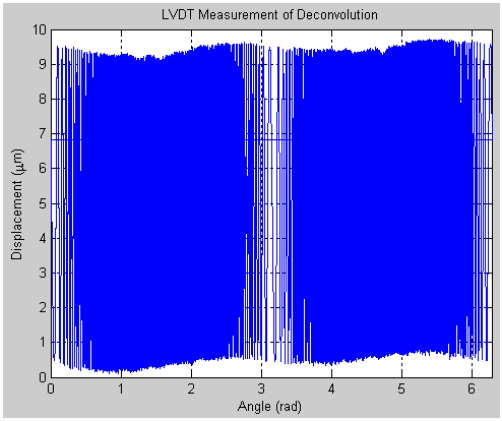

Figure 13. Swept sine wave using deconvolution technique.

test the quality of the machined sine waves and the results are shown in Figure 13.

Figure 13 was measured using an air-bearing LVDT mounted to the base of the DTM as shown in Figure 6. The spindle was driven at a low speed (2 RPM) and the resulting data has been modified to compensate for the 1 mm diameter of the LVDT tip. This compensation is needed because the tip radius is large with respect to the features of the sine wave and the data from the LVDT will provide a distorted picture of the machined sine waves. The tip radius will appear to increase the width of the sine waves and reduce the distance between them. The decreases in amplitude present in the previous measurement of the machined surfaces are now gone. The problem was that the LVDT probe could not penetrate to the bottom of the valleys because the wavelength was too small. The features in Figure 13 had a wavelength from 6.4 mm to 0.371 mm. The previous swept sine wave in Figures 8 and 10 went from 4.82 to 0.186 – a significant difference. There are still some problems with the features in Figure 13 and additional work will be done to improve the fidelity of the surface shape.

8.6 FUTURE WORK

The closed loop control with deconvolution will be used to cut more swept sine waves on a cylinder. Based on the results of this fabrication, the technique will be finalized and implemented in the manufacture of the final artifact. Additional development is needed to finalize a mounting procedure to reduce the distortion of the ring. The last phase of the project includes uncertainty analysis. Once the ring gauge has been made, it needs to be measured to determine accurate information of the geometry and features of the ring. This accepted data will be used for comparison purposes with the results taken on various CMMs at Y-12.

REFERENCES

1. Cauchick-Miguel, P., King, T., Davis, J., *CMM verification: a survey*. Measurement, 1996, 17 (1), p. 1-16.

2. Balkey, M.M., Day, R.D., Batha, S.H., Elliot, N.E., Pierce, T., Sandoval, D.L., Garrard, K.P., and Sohn, A., *Production and Metrology of Cylindrical Inertial Confinement Fusion Targets with Sinusoidal Perturbations*. Fusion Science and Technology, Vol 45, No 2, p. 107-112, (2004).

3. Panusittikorn, W. *Error Compensation using Inverse Actuator Dynamics.* PhD Dissertation, NC State University, August 2004.

9 HIGH PRESSURE PHASE TRANSFORMATION AND DUCTILITY IN DIAMOND TURNED SILICON

Travis Randall
Graduate Student
Dr. Ronald Scattergood
Professor
Department of Materials Science and Engineering

9.1 INTRODUCTION

It has been well documented that single crystal silicon and germanium undergo phase transformation with the generation of high pressure on the surface by contact processes such as micro-indentation, scribing, and single point diamond turning. Investigations of the transformation region created report phase transformation from diamond cubic (dc) structure to the amorphous structure. The transformation to the metallic beta-tin phase is thought to be responsible for anomalous plastic flow behavior without fracture seen in contact loading processes. The beta-tin phase is not generally seen at room temperature or pressure but is rather identified by an amorphous phase or R8/BC8 crystal structure seen after material unloading, depending on experimental conditions. [1]

The implication of the ductile behavior is, that using careful machining conditions, single crystal silicon may be ground or diamond turned in the ductile regime. Ductile machining will reduce cracks and dislocations generated by machining on the surface and subsurface regions that can reduce the mechanical integrity and lower the operation lifetime of the components. The mechanisms governing the material removal (a combination of microcracking, dislocation motion, and structure change- HPPT) in ductile-regime turning are not well understood. The work presented here is mainly focused on the appearance of amorphization (structure change) in a ductile-turned region. Secondary focus is placed on the characterization of surface finish and cutting behavior as a function of crystallographic orientation and cutting direction, feed rate, and rake angle.

9.2 PROJECT DETAILS

A Rank Pneumo ASG 2500 Diamond Turning Machine is used to turn various orientations of single crystal silicon wafers at room temperature as a function of feed rate (1-15 um/rev) and tool rake angle (-30^{o} and -45^{o}) with a large radius (3mm) round-nosed tool.

Characterization of the machined surface was accomplished with Macro-Raman spectroscopy done at room temperature using an ISA U-1000 scanning monochromator. Raman excitation was done with the 514.5 nm line of an Argon-ion laser, with a spot size of approximately 1mm in diameter. Raman spectra were taken in the 200-600 cm^{-1} range, which contains the characteristic peaks normally associated with crystalline, amorphous, and various metastable crystalline phases seen in other research. A spectral resolution of ≈ 4 cm^{-1} was utilized, and the laser power was ≈ 5 mW.

Surface finishes of the ductile-turned regions were measured using a Zygo New View 5600 white light interferometer. MetroPro, the software suite used to analyze the interferometer data, reports a measure of surface roughness by the root mean square (RMS) parameter and peak to valley (PV) values. Measurements were taken for from the center outward in regions within and outside the predicted fracture pattern area (further explained in Results section.)

9.3 EXPERIMENTAL RESULTS

Optical quality, low RMS surfaces (1-10 nm) where created by single point diamond turning single crystal Si wafers in the ductile regime. Ductile regime material removal was evident by the absence of fracture damage and repeated feed marks in the surface as well as generation of continuous chips. Increasing feed rate seemed to create an increase in surface roughness as shown in Figure 1.

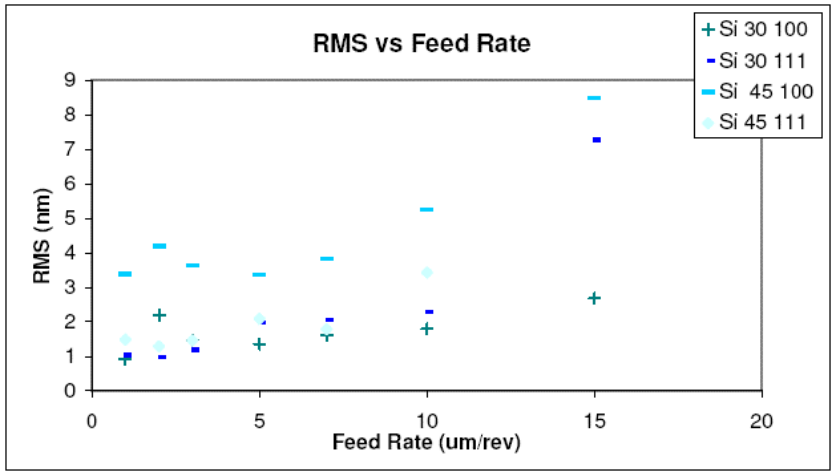

Figure 1. RMS vs. Feed Rate for various feed rates on single crystal silicon.

Feed rate seemed to be the limiting factor for generating a damage free surface. At increasing feed rates, certain directions on a wafer face initiated fracture before others, creating symmetric damage patterns on the surface. The more negative rake angle tool tended to suppress the onset of fracture in the favored direction allowing machining at higher feed rates. The damage patterns

for the wafer orientations tested ((100), and (111)) were very similar to those found previously and were explained qualitatively by an orientation stress model used in that research. [2] These are shown in Figure 2.

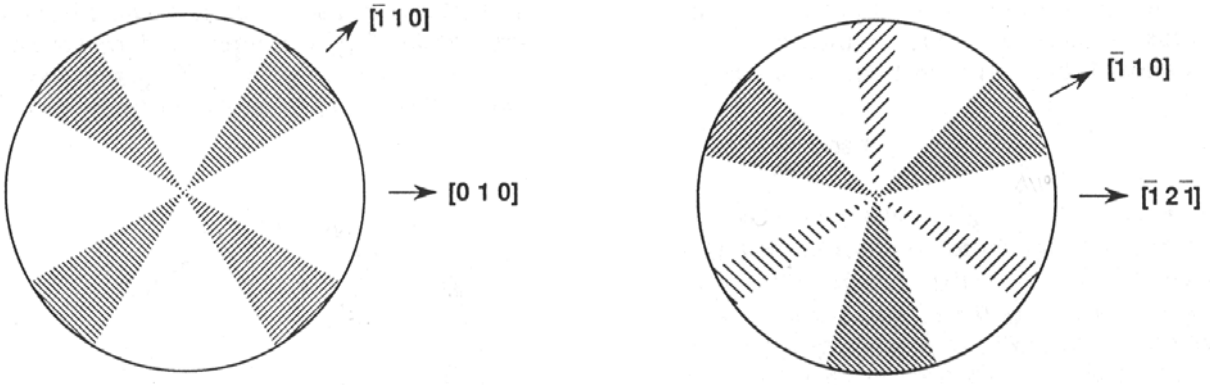

Figure 2. Damage patterns for (100) and (111) wafers resultant from machining at sufficiently high feed rates. [2]

Oddly, for surfaces that where ductile turned with similar parameters of tool rake and low feed rate, there appeared to be no difference in surface roughness and profile shape radially (changing cutting direction) as measured by interferometery methods.

The RMS (and PV) value of ductile turned surfaces was limited by the effect of the condition of the tool tip. While tips were freshly sharpened, experimental preparation (i.e. part touch off and preliminary facing cuts) perhaps dulled the tips enough to result in non-ideal material removal (deformation under the tool and elastic spring back.) This was evident by higher-than-theorized PV values, and machining profiles that did not fit theoretical shape (but were similar to realistic expectations) as measured by interferometery techniques. Additionally, machining runs on Si were subject to tip wear and damage considerations as evident by the repeated patterns of tip damage features into the part surface. Despite these various problems, surfaces turned within the ductile regime had RMS values in the range of <1 nm to 10 nm increasing with feed rate.

Raman measurements of the ductile turned surfaces for various machining conditions indicated what is thought to be the presence of a near-surface amorphous layer. The presence of this layer is thought to be a remnant of a rapid back transformation from the beta-tin metallic phase. The most noticeable trend for each of the parameters tested is the drastic decrease in amorphous intensity coupled with an increase in dc peak intensity when switching feed rates from 1 to 5μm/rev. While the Raman measurements did not always clearly indicate the existence of this layer for samples machined at 5um/rev, closer inspection showed the possibility of an amorphous peak existence. It is thought that the layer may still be present but the thinning layer may be

more difficult to detect. There seems to be no direct evident difference in amorphous signal intensity between crystal orientations, cutting direction, or rake angle as seen in Figures 3-8.

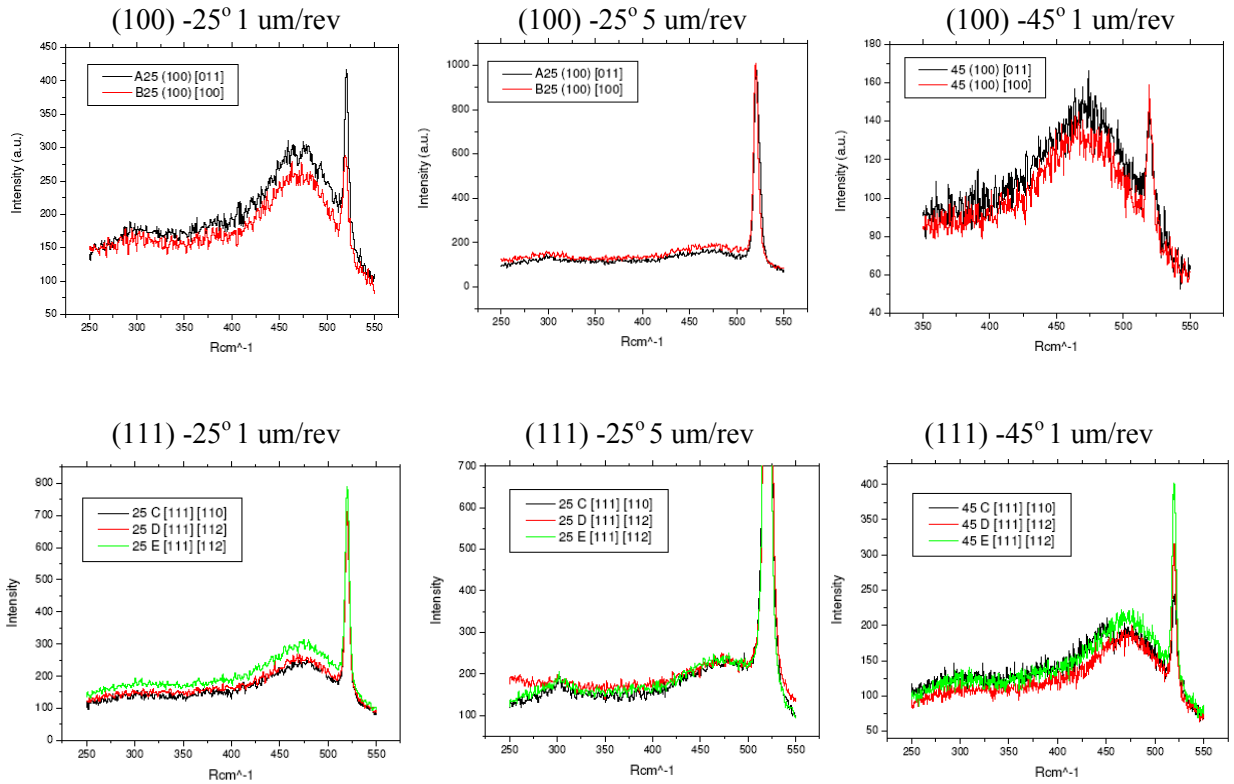

Figures 3-8. Raman spectra for various conditions taken on ductile turned surfaces showing heavy dependence of amorphous/dc intensity ratio on feed rate, but little else.

TEM results (Figure 9 and 10) showed that the chips studied by diffraction are thought to be of dc crystal structure. Si chips generally showed morphology of smaller (1-2 um) clustered chips. Despite the amorphous nature of the near surface machine regions, TEM failed to show direct evidence of the amorphous nature of the chip. It is thought that intense local heating during machining may cause recrystallization of the amorphized material, as the thin chips lack cannot dissipate heat quickly.

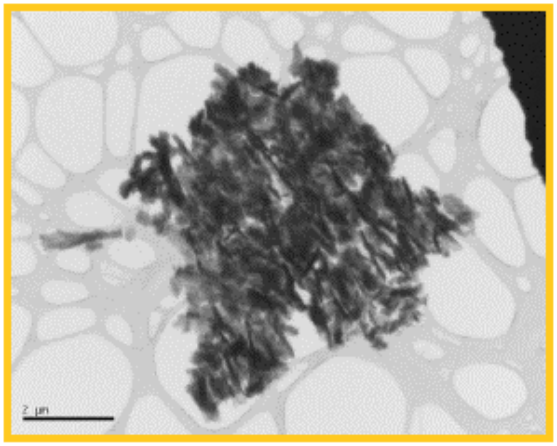

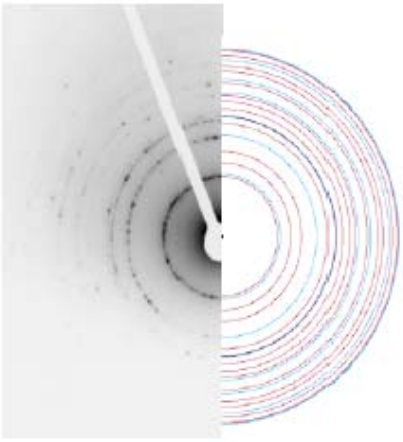

Figures 9 and 10. TEM image of Silicon chip generated during ductile regime turning and corresponding electron diffraction pattern showing crystalline structure of chip.

9.4 CONCLUSIONS

Low RMS surfaces were achieved by ductile regime turning with high negative rake, large radius round nosed tools for various crystallographic orientations of single crystal silicon. Symmetric fracture patterns resulting from high feed rate machining were the limiting factor for ductile regime machining. Surface characteristics such as roughness and profile seemed to show little dependence on cutting direction within the ductile regime. Raman measurements indicated the presence of a near surface amorphized layer for regions where ductile turning occurred. This is thought to be the remnant of a back transformation from the metallic beta-tin phase, which is responsible for the ductile behavior during machining. TEM analysis of the chips was shown to be crystalline in nature possibly indicating rapid recrystallization of the amorphous surface layer upon removal.

9.5 FUTURE WORK

Future work includes cross-sectional TEM of machined regions to show definitively the effect of the various parameters on the amorphized layer thickness, as well as the underlying damage to the dc material. Additionally, further diamond turning and Raman experiments are planned.

REFERENCES

1. Domnich, V. and Y. Gogotsi. “Phase Transformations In Silicon Under Contact Loading”, Rev.Adv.Mater.Sci. 3 (2002) 1-36

2. Blackley, W.S. and R.O. Scattergood. “Crystal Orientation and Dependence of Machining Damage- A Stress Model.” J. Am. Ceram. Soc., 73[10], 3113 (1990).

10 DESIGN TOOLS FOR FREEFORM OPTICS

Kenneth P. Garrard
Research Associate
Thomas A. Dow
Professor
Department of Mechanical and Aerospace Engineering

10.1 INTRODUCTION

Advanced optical systems play a pivotal role in military applications including advanced optical telescopes and imaging LADARs (laser detection and ranging). Optics provides the eyes for surveillance, detection, tracking and discrimination. Therefore, improvements in optical design and fabrication are important targets for research and development efforts. One such improvement is the inclusion of freeform elements in the optical design. A recent NASA imaging spectrometer (IRMOS) utilized freeform surfaces to help reduce the size of the system by an order of magnitude [1]. Significant reductions in size can dramatically reduce the use of exotic materials such as beryllium. The ensuing mass reductions provide enhanced performance for space systems and interceptors that require high accelerations in order to reach their targets at the correct point in trajectory. Freeform surfaces can also be utilized to control astigmatism at multiple locations in the field of view and thus reduce wavefront aberration.

To make these advanced optical systems available for commercial and defense applications, an enhanced design environment is needed; one that gives the designer feedback on the manufacturability of the design as well as the optical performance. This environment needs a fundamentally new figure of merit to simultaneously predict optical performance and fabrication complexity. The kernel of this design environment is the subject of a Phase I STTR that has recently been funded by the Missile Defense Agency (MDA).

The goal for this project is the creation of optical design software that, for the first time, optimizes both traditional optical performance measures and new manufacturing specific process metrics to leverage recent advances in design and fabrication capabilities for freeform optical components. Coupled with existing commercially available optical design capabilities, this new software will enable optical system designers to deploy cost effective freeform surface shapes (through minimization of optical design effort, manufacturing setup and machining time) for use in advanced multi-band (IR and visible) imagery systems. Designers will be able to create advanced optical systems to meet the evolving requirements of MDA while ensuring that they are producible. This project will combine the capabilities of the foremost optical design house,

Optical Research Associates (ORA), with the unique freeform design, fabrication and metrology experience of the Precision Engineering Center (PEC).

10.2 OPTICAL DESIGN FOR MANUFACTURING

This project involves the transfer of technology from the PEC to ORA with the goal of providing the optical designer with timely feedback on the manufacturing feasibility and cost of design options. By incorporating knowledge of the capabilities and limitations of fabrication technologies into the design optimization software, the class of available surfaces can be extended to include freeform geometries. Initially the scope of this work is limited to diamond machining with a fast tool servo and off-axis conic surfaces.

10.2.1 OPTICAL DESIGN

The selection of elements and element locations for a new optical design is driven by optical performance and packaging requirements. The designer can employ reflective, refractive or diffractive elements whose shapes can be plano, spherical, aspherical or freeform. However, once an acceptable design is conceived, manufacturing and assembly issues determine its viability. The cost to change the design is lowest in the early stages and is increasingly expensive as the effort proceeds from concept to product. If the designer has feedback on the manufacturability of the elements early in the design process, the quality of the final design can be improved.

For a design that consists of a series of spherical elements, a large body of information is available regarding manufacturability – material compatibility, geometry limitations, delivery and cost. Aspheric designs are less common but fabrication capabilities to generate such surfaces are available. However, freeform surface fabrication capabilities are very limited. While some of the available optical software can deal with such shapes, no feedback is available to the designer on either the feasibility or the cost to create such a surface. Hence, most designers tend to avoid freeform shapes, even if they would simplify the design, reduce the number of components, improve the imaging performance, shorten the assembly time, and decrease the cost.

10.2.2 FABRICATION

Freeform optical surfaces have no axis of symmetry and, as a result, this surface shape is a function of both radius (r) and angular position (θ). To produce such a surface, an additional degree of freedom is needed. This has been done by driving the machine tool axis as a function of r and θ (typically a big, heavy axis and thus the spindle speed must be very low and production time is excessive) or adding an auxiliary axis (Fast Tool Servo - FTS) to move the

tool. Auxiliary axes can be obtained with strokes from 5 µm to several mm and operating frequencies from 1 KHz to 2 Hz respectively.

A fast tool servo on a Diamond Turning Machine (DTM) is the most efficient way to produce freeform shapes in diamond turnable materials. The FTS can be programmed to create surfaces that are a function of DTM axes positions as well as the spindle angular position as illustrated in Figure 1. The shape of the freeform part can be divided into rotationally symmetric and Non-Rotationally Symmetric (NRS) components as illustrated in Figure 2 and the decomposition can have a major impact on the fabrication process. The creation of these two components (not necessarily unique) is a technical challenge that has been addressed at the Precision Engineering Center (PEC) at NC State University and will be incorporated in this project [2].

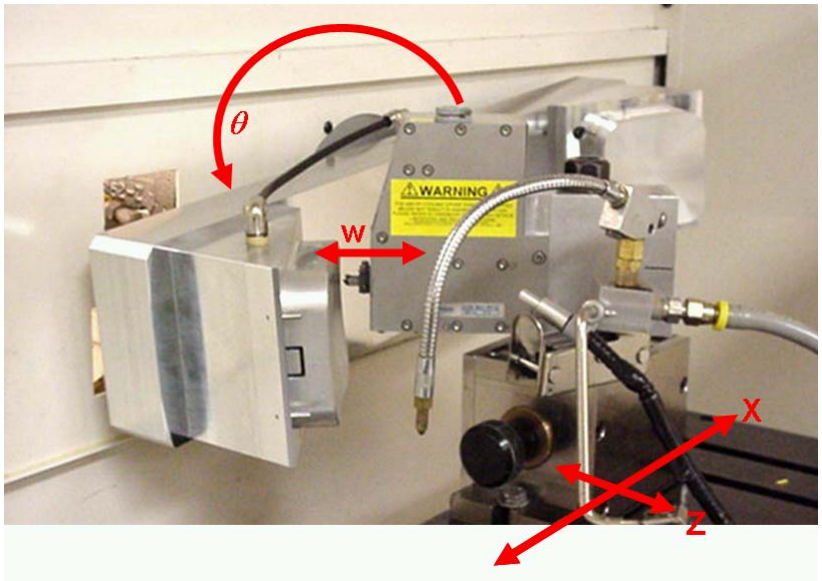

Figure 1. Coordinate system for machining an off-axis freeform surface with a fast tool servo.

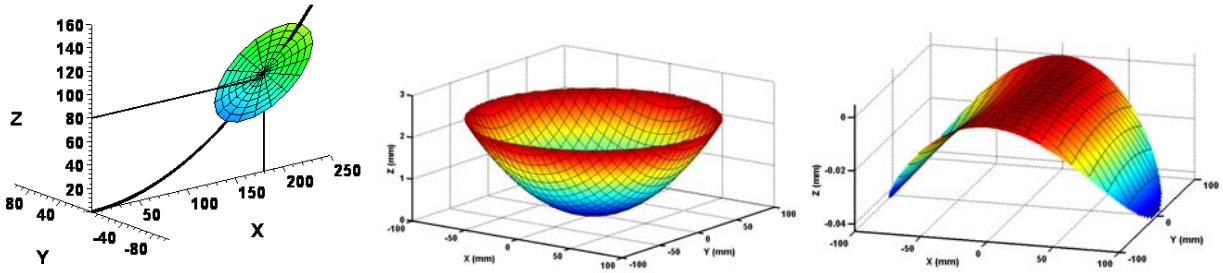

Figure 2. Off-axis conic segment (a), and its decomposition into symmetric (b) and non-symmetric (c) components for machining on-center. Note the 100x increase in amplitude scale for the non-symmetric component.

The main axes of the DTM (X and Z) create the symmetric component (function of radius, r) while the FTS adds the non-symmetric component (function of angular location, θ, as well as radius, r). As the tool feeds from the outside of the part to the center, the linear axes of the lathe move the tool along the correct asphere (Figure 2b) and the fast tool servo simultaneously moves the tool in the W direction to add the (r, θ) component (Figure 2c) that will create the desired optical shape (Figure 2a). The range and bandwidth of the FTS will dictate the feed rate and maximum spindle speed, which will have a direct bearing on the time and cost to fabricate the surface.

10.2.3 ASTIGMATISM FROM OBLIQUE RAYS

An optical wavefront acquires aberration, especially astigmatism, when it reflects obliquely off a curved mirror that is locally rotationally symmetric. This means that the surface is rotationally symmetric about the normal vector at a point intersected by the central ray in the beam. Because of the obliquity, the mirror appears to have more power in the direction of the field angle. A fan of rays in the plane of the field angle will focus closer to the mirror than a fan of rays in the orthogonal direction. The axial separation of the best focus for horizontal and vertical ray fans is a measure of astigmatism. For a locally rotationally symmetric mirror, a field angle whose chief ray is coaxial with the mirror axis (normal incidence) is the only field angle where there is no astigmatism. Otherwise, astigmatism increases as the square of the field angle. Controlling astigmatism in systems with off-axis fields can be accomplished by including one or more non-rotationally symmetric elements in the design. This usually results in a more compact optical layout as well.

10.2.4 BENEFITS OF FREEFORM SURFACES

To avoid astigmatism at a single off-axis field angle, what is needed is a locally anamorphic surface (i.e., not rotationally symmetric about the local surface normal), with a longer radius in the field angle direction than in the orthogonal direction. With an off-axis field, replacing a rotationally symmetric surface with a freeform surface allows the vertical and horizontal fans of rays to focus at the same point. Figure 3 shows a representative unobscured mirror system with associated astigmatism maps across the extended field of view for both the locally rotationally symmetric and freeform versions of the system. The length of the lines in the figure indicates the magnitude of the astigmatism. Note there are two nodes (points where the aberration is zero) in the field. In this illustration, one can zero out the astigmatism for two off axis field angles (mirror images of each other), but for a range of field angles one cannot exactly zero the astigmatism. Distortion and coma also have this nodal behavior. Thus a key benefit of using freeform surfaces is that they offer the designer the ability to control both the number and position of aberration nodes within the field of view. This level of control allows us to reduce the worst-case wavefront aberration.

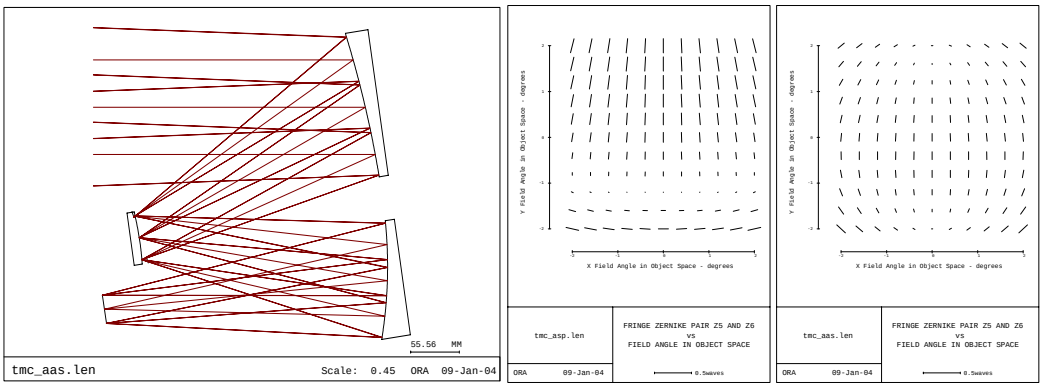

Figure 3. Optimized image quality for a 3-mirror anastigmat imager (left) has more than twice as much astigmatism across the full-field using symmetric surfaces (center) as can be achieved with freeform surfaces (right).

10.2.5 MODELING FREEFORM SURFACES

There are at least two ways to model locally anamorphic power. One is to take an axially symmetric surface and add tilt, decenter, and asphericity. In that case the vertex of the surface may be far off of the working aperture and the tilt angle may be large. However, it is simpler and more efficient to model the surface without such an extreme tilt and decenter. This can be accomplished by modeling the surface directly as an anamorphic function such as an aspheric toroid. This method of modeling can also help the fabrication process. The freeform surface can be thought of as decomposition into an axially symmetric surface plus NRS deformations. If the axis of symmetry of the rotationally symmetric portion is in or near the working aperture, then fabrication is easier using a spindle-based method in which the part rotates about an included axis.

10.2.6 OPTIMIZATION MERIT FUNCTIONS

When a freeform surface is to be utilized, the designer needs tools to evaluate the feasibility and cost of manufacture. The designer also requires techniques for quantifying these criteria, so they can be incorporated into an optimization strategy that permits simultaneous control of manufacturing issues and overall optical quality. The mathematical foundation for evaluating manufacturing cost has been developed at the PEC for off-axis conic surfaces to be machined on-center [3].

This algorithm decomposes the surface into a best-fit aspheric shape and a nonrotationally symmetric component that together create the required surface. The algorithm attempts to minimize the sag of the non-rotationally symmetric component to limit the dynamic range of the fast tool servo and maximize machining speed. In its current form, this software can be used to

analyze an existing design, but it cannot be included in the optimization process to facilitate the generation of improved optical designs.

The project objective is to create new software algorithms that tie together the mathematical surface decompositions for machining off-axis conic sections that are machined on-center using a FTS with the optical design environment using automated optimization techniques. To accomplish this, fundamental relationships must be discovered that will allow the creation of merit functions to be used within the optimization environment to produce the best (in terms of manufacturability and cost) decomposition of the symmetric and asymmetric components of the desired surface shape. This research will quantify the freeform optical manufacturing processes and create a new capability in optical computer aided design (OCAD) software tools to support manufacturing. The software developed will be the foundation for a future effort to prototype a working optical system that includes freeform elements.

The algorithms and design environments to be explored during this effort will assist an optical designer in the development of freeform optical components by providing timely feedback on the feasibility of fabrication. The class of optics to be addressed is freeform optics that can be machined using a fast tool servo. The software will:

- Provide feedback on the FTS range of motion required to machine the optical surface,
- Compare the range to available diamond turning machine systems,
- Estimate the fabrication time,
- Incorporate manufacturing parameters into the optical optimization process, and
- Produce output files that decompose the surface into best-fit asphere and NRS parameters suitable for downloading to a manufacturing process.

10.3 PLAN OF WORK

The project will develop an integrated design and optimization environment that brings together, for the first time, the existing optical performance predictions with automated feedback of manufacturing costs of FTS machined freeform surfaces. Schematically, the project will create the environment shown in Figure 4.

The proposed work plan is intended to prove the feasibility of practical and cost effective use of freeform surfaces for off-axis systems, where such surfaces would produce substantially less spherical aberration, astigmatism, distortion, coma and higher order aberrations such as trefoil and oblique spherical aberration. These surfaces would also enable the design of systems with lower overall wavefront error. To accomplish this goal, algorithms to enable process-aware optimization of optical performance will be created by first decomposing freeform surfaces into axially symmetric and anamorphically deformed component shapes and then controlling those

shapes using manufacturing metrics though a set of intrinsic functions. Once this task is completed, novel verification and visualization methods must be created that will quantify the quality of the resulting surface manufacture. Each of these accomplishments will require innovation. The technical risks of creating a viable design and manufacturing process that will provide the imaging benefits of freeform surfaces are substantial, due primarily to the challenge of developing metrics that quantify the manufacturing impacts in ways that allow the metrics to be used effectively with existing, highly quantitative metrics such as image quality. As discussed, the benefit of using freeform surfaces in the design of unobscured mirror systems, typical of systems designed for surveillance, target detection, tracking and discrimination, is to reduce the overall level of aberrations in the system.

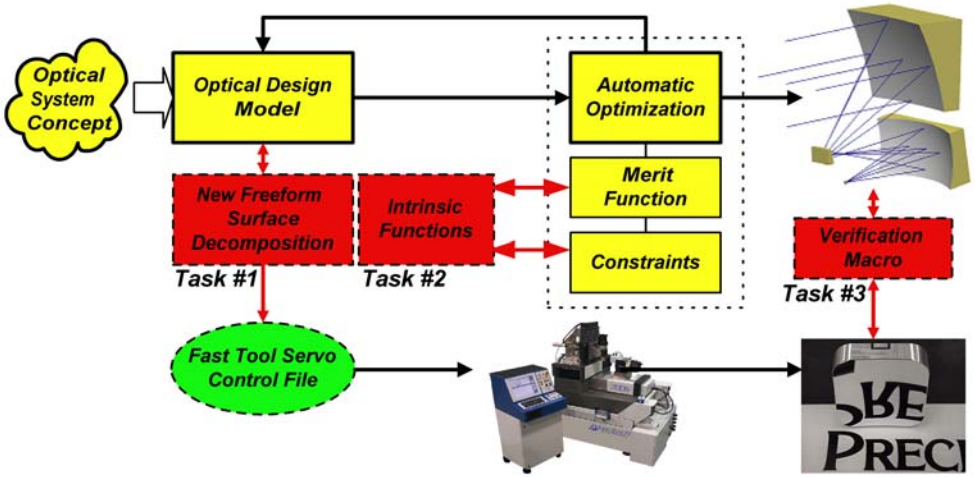

Figure 4. Integration of freeform surface decomposition with automatic optimization.

REFERENCES

1. Garrard, K., A. Sohn, R. G. Ohl, R. Mink, V. J. Chambers. "Off-Axis Biconic Mirror Fabrication", *Proceedings from the EUSPEN 2002 Annual Meeting* (2002).

2. United States patent 5,467,675. Apparatus and method for forming a workpiece surface into a non-rotationally symmetric shape. Thomas A. Dow, Kenneth P. Garrard, George M. Moorefield, II and Lauren W. Taylor (1995).

3. Allen, W.D., R.J. Fornaro, K.P. Garrard and L.W. Taylor. "A high performance embedded machine tool controller", *Microprocessors and Microprogramming*, **40**, 179-191, (1994).